

Scott K. Rowland · Andrew J. L. Harris ·
Martin J. Wooster · Falk Amelung · Harold Garbeil ·
Lionel Wilson · Peter J. Mougini-Mark

Volumetric characteristics of lava flows from interferometric radar and multispectral satellite data: the 1995 Fernandina and 1998 Cerro Azul eruptions in the western Galápagos

Received: 8 March 2002 / Accepted: 18 November 2002 / Published online: 5 April 2003
© Springer-Verlag 2003

Abstract We have used a suite of remotely sensed data, numerical lava flow modeling, and field observations to determine quantitative characteristics of the 1995 Fernandina and 1998 Cerro Azul eruptions in the western Galápagos Islands. Flank lava flow areas, volumes, instantaneous effusion rates, and average effusion rates were all determined for these two eruptions, for which only limited syn-eruptive field observations are available. Using data from SPOT, TOPSAR, ERS-1, and ERS-2, we determined that the 1995 Fernandina flow covers a subaerial area of $6.5 \times 10^6 \text{ m}^2$ and has a subaerial dense rock equivalent (DRE) volume of $42 \times 10^6 \text{ m}^3$. Field observations, ATSR satellite data, and the FLOWGO numerical model allow us to determine that the effusion rate declined exponentially from a high of $\sim 60\text{--}200 \text{ m}^3 \text{ s}^{-1}$ during the first few hours to $< 5 \text{ m}^3 \text{ s}^{-1}$ prior to ceasing after 73 days, with a mean effusion rate of $4\text{--}16 \text{ m}^3 \text{ s}^{-1}$.

Integrating the ATSR-derived, exponentially declining effusion rate over the eruption duration produces a total (subaerial + submarine) DRE volume of between 27 and $100 \times 10^6 \text{ m}^3$, the range in values being due to differing assumptions about heat loss characteristics; only values in the higher part of this range are consistent with the independently derived subaerial volume. Using SPOT, TOPSAR, ERS-1, and ERS-2 data, we determine that the 1998 Cerro Azul flow is 16 km long, covers 16 km^2 , and has a DRE volume of $54 \times 10^6 \text{ m}^3$. FLOWGO produces at-vent velocity and effusion rate values of 11 m s^{-1} and $\sim 600 \text{ m}^3 \text{ s}^{-1}$, respectively. The velocity value agrees well with the 12 m s^{-1} estimated in the field. The mean effusion rate (total DRE volume/duration) was $7\text{--}47 \text{ m}^3 \text{ s}^{-1}$. Dike dimensions, fissure lengths, and pressure gradients along the conduit based on magma chamber depth estimates of 3–5 km produce mean effusion rates for the two eruptions that range over nearly four orders of magnitude, the range being due to uncertainty in the magma viscosity, dike dimensions, and pressure gradient between magma chamber and vent. Although somewhat consistent with mean effusion rates from other techniques, their wide range makes them less useful. The exponentially declining effusion rates during both eruptions are consistent with release of elastic strain being the driving mechanism of the eruptions. Our results provide independent input parameters for previously published theoretical relationships between magma chamber pressurization and eruption rates that constrain chamber volumes and increases in volume prior to eruption, as well as time constants of exponential decay during the eruption. The results and theoretical relationships combine to indicate that at both volcanoes probably 25–30% of the volumetric increase in the magma chamber erupted as lava onto the surface. In both eruptions the lava flow volumes are less than 1% of the magma chamber volume.

Editorial responsibility: T. Druitt

S. K. Rowland (✉) · A. J. L. Harris · F. Amelung · H. Garbeil ·
L. Wilson · P. J. Mougini-Mark
HIGP/SOEST, University of Hawai'i,
2525 Correa Road, Honolulu, Hawai'i 96822, USA
e-mail: scott@higp.hawaii.edu
Tel.: +1-808-9563150
Fax: +1-808-9566322

A. J. L. Harris
Department of Earth Sciences, The Open University,
Milton Keynes, MK7 6AA, UK

M. J. Wooster
Department of Geography, King's College London,
University of London, Strand, London, WC2R 2LS, UK

L. Wilson
Environmental Science Department,
Lancaster University, Lancaster, LA1 4YQ, UK

Present address:

F. Amelung, Marine Geology and Geophysics/RSMAS,
University of Miami, Rickenbacker Causeway 4600,
Miami, FL 33149, USA

Keywords Effusion rate · Galápagos · Magma chamber ·
Numerical modeling · Remote sensing

Introduction

Reliable measurements of lava flow volume and effusion rate are important for analyzing effusive activity at a volcano. For example, volumetric data for individual flows contribute to cumulative volumetric time series (e.g., Lipman 1995; Rowland 1996), and changes in the rate of lava accumulation indicate variations in eruptive behavior (Wadge 1977; Crisp 1984; Holcomb 1987; Moore and Mark 1992; Dvorak and Dzurisin 1993). Similarly, variations in effusion rate during an effusive event provide insights into processes occurring within the shallow plumbing system (e.g., Wadge 1977, 1981; Rowland and Walker 1990; Dvorak and Dzurisin 1993), as well as the likely hazard to down-flow communities (e.g., Barberi et al. 1993; Kauahikaua et al. 1995; Trusdell 1995). For most eruptions on most volcanoes only the mean effusion rate, attained from the total flow volume divided by the eruption duration, is available. However, because effusion rates often vary significantly during an eruption, for example due to elastic strain release in the magma chamber (Wadge 1981), instantaneous effusion rates determined at more than one time during an eruption are more useful. It is notoriously difficult, however, to determine instantaneous effusion rates in the field (see review by Pinkerton 1993), and indeed only one field estimate was made for each of the two eruptions considered here. Another useful quantity is the peak effusion rate that is commonly achieved during the initial hours or days of an eruption.

Recent advances in remote sensing allow flow area, flow volume, plus mean and instantaneous effusion rates to be measured from space. For example (Rowland et al. 1999; Stevens et al. 1999), flow volumes can be determined by comparing pre- and post-eruption digital elevation models (DEMs) such as those derived from

Interferometric Synthetic Aperture Radar data (InSAR; Zebker and Goldstein 1986). We also have the ability to detect changes in flow area during an eruption by mapping out regions where the surface has changed to the extent that two radar images decorrelate (e.g., if a new flow is emplaced; Zebker et al. 1996). Instantaneous effusion rates can be obtained from thermal infrared satellite images using a thermal budget model (e.g., Harris et al. 1997, 1998). An advantage of this technique is the relatively high temporal resolution of some of the satellites that carry thermal infrared imagers. Such temporal resolutions range from 16 days for the Landsat sensor to ~6 h for the Advanced Very High Resolution Radiometer (AVHRR) to 15 min for the Global Observational Earth Satellite (GOES; Harris et al. 2001, 2002a, 2002b).

A numerical thermo-rheological model, FLOWGO (Harris and Rowland 2001), allows us to input at-vent effusion rates and compare the modeled flow lengths and velocities with mapped and observed flow lengths and velocities. FLOWGO provides an additional constraint on the eruption parameters during the event.

We used the satellite- and model-derived effusion rates to quantify the 25 January–8 April 1995 eruption of Fernandina and the 15 September–21 October 1998 eruption of Cerro Azul, both of which are in the W. Galápagos Islands (Fig. 1). Both eruptions have already been the topic of remote sensing studies that use single data sets (Wooster and Rothery 1997; Jonsson et al. 1999; Amelung et al. 2000; Mouginiis-Mark et al. 2000). We combine those observations, collected by GOES, plus the Synthetic Aperture Radar (SAR) and Along Track Scanning Radiometer (ATSR; Mutlow et al. 1999) aboard the European Remote Sensing Satellites (ERS-1 and -2), with InSAR from the airborne TOPSAR as well as FLOWGO and other modeling results. These data allow us to derive lava flow volumes, volumetric eruption rates,

Fig. 1 Location map of the Galápagos Islands (adapted from a map published by Libreria Internacional, Quito, Ecuador). The subaerial contour interval is 200 m, and the contours for Fernandina and Isabela Islands are from TOPSAR. Bathymetric contours (generalized) are at 100 m and then in multiples of 1,000 m. *PV* indicates Puerto Villamil, the only established human habitation on either Isabela or Fernandina

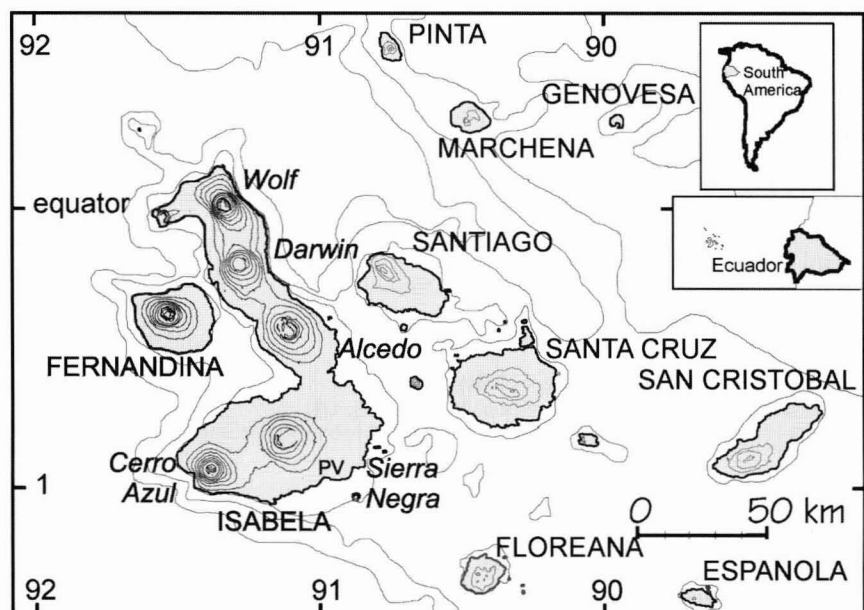
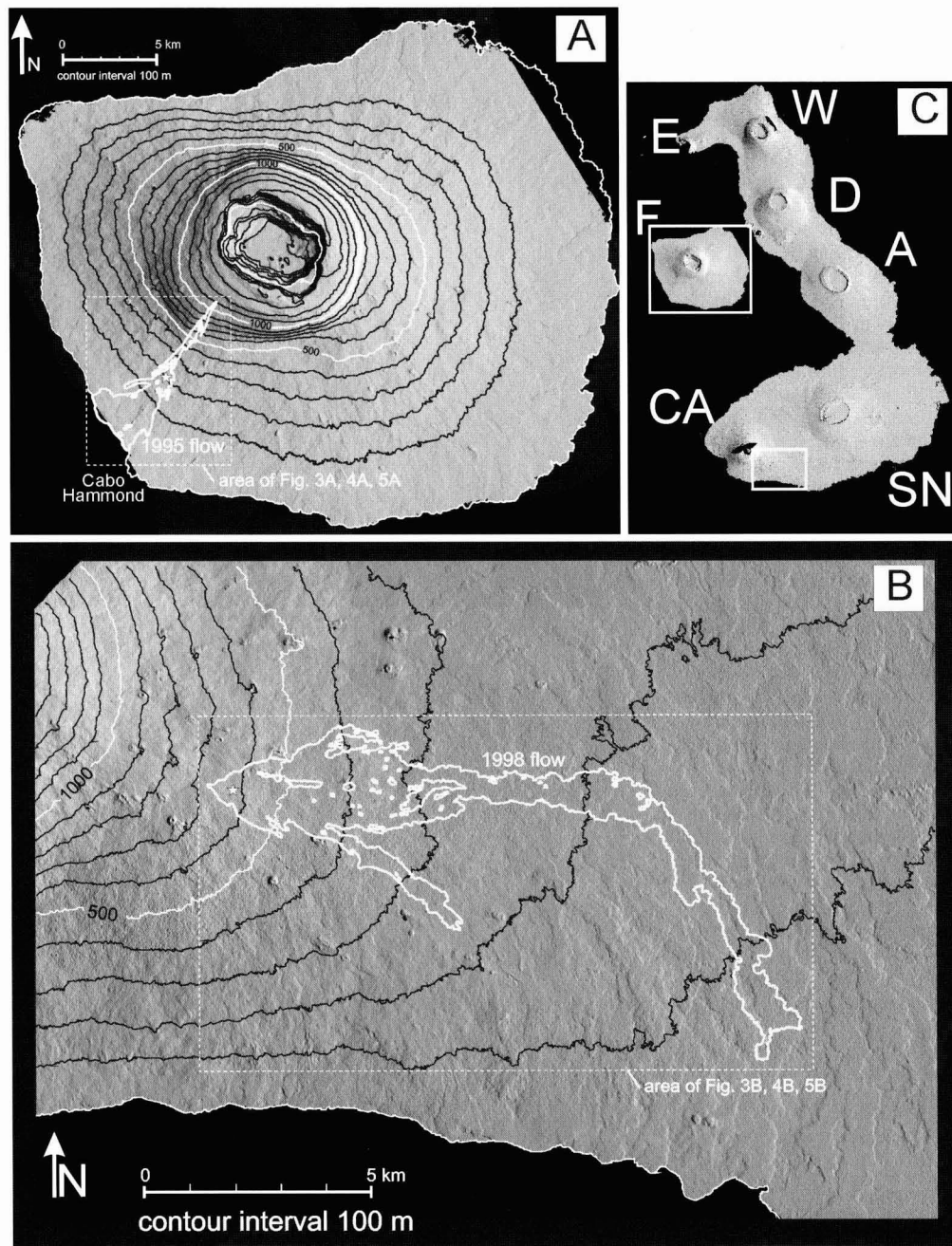


Fig. 2 Shaded relief images showing the locations of the **A** 1995 Fernandina and **B** 1998 Cerro Azul eruptions. Topographic data are from TOPSAR, collected in May of 1993. *Boxes* in **A** and **B** show locations of subsequent figures. *Stars* indicate approximate locations of main vents. *Boxes* in **C** show locations of **A** and **B**



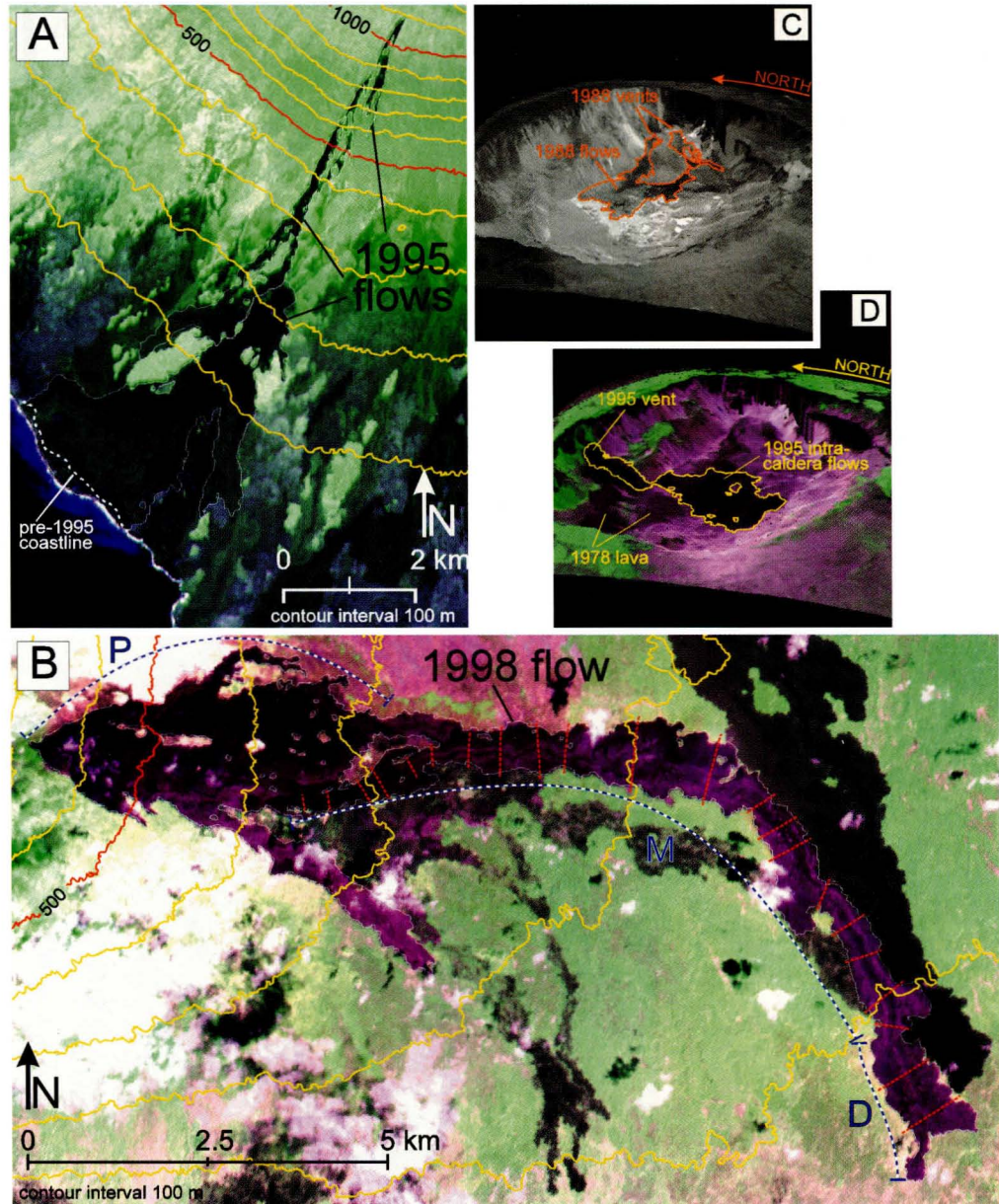
and effusion rates for these two recent eruptions that were otherwise not closely monitored. Elastic release of strain from a filled magma chamber has been proposed as a significant driving force for volcanic eruptions (e.g., Wadge 1981). In such a case the effusion rate is expected to show an exponential decline over the duration of the eruption. Published theoretical relationships relate exponentially declining effusion rates to magma chamber parameters such as volume, volume change, and pressure (Wadge 1981; McTigue 1987). Because our effusion rate data were acquired independently of these models we are in a position to assess the models and use them to

determine the magma chamber properties at Fernandina and Cerro Azul.

The western Galápagos volcanoes

The Galápagos volcanoes (Fig. 1) are basaltic shields noted for their relatively unusual morphology (e.g., McBirney and Williams 1969; Simkin 1972). Cerro Azul is the SE-most of six volcanoes comprising Isla Isabela whereas Fernandina is a single-volcano island (Fig. 1). As described in Naumann and Geist (2000) and in Rowland and Garbeil (2000), flow mapping combined with slope

Fig. 3A–D Color SPOT images of both eruption sites (see boxes on Fig. 2A, B for locations). **A** Fernandina data collected 6 July 1995 are bands 3 (near-IR), 2 (red visible), and 1 (green visible) projected in red, green, and blue, respectively. **B** Cerro Azul data collected 16 December 1998 are bands 1 (green visible), 4 (near-IR), and 2 (red visible) projected in red, green, and blue, respectively. *Dashed red lines* in **B** are locations of channel and flow width measurements presented in Fig. 9A, and *P, M, and D* indicate proximal, medial, and distal portions of the flow (see text). **C, D** Panchromatic and color SPOT images showing the Fernandina caldera before and after the 1995 eruption (25 October 1988 and 6 July 1996, respectively), produced by draping SPOT data over the 1993 TOPSAR DEM and viewed toward the east. Note that the statement by Rowland (1996) that no new flows are visible in the caldera is in error; 1995 intra-caldera flows erupted from a vent at the eastern end of the NW bench and flowed southward onto the caldera floor. Other flows on the NW bench that appear to be new are 1978 lavas that are obscured by dust generated during an avalanche that occurred ~5 weeks prior to the 1988 image (Chadwick et al. 1991; Rowland and Munro 1992)



data obtained from InSAR-derived DEMs have already contributed to the study of these morphologies. The W. Galápagos volcanoes are regularly active, with ~60 eruptions reported since the early 1800s (Simkin and Seibert, 1994). Reynolds et al. (1995) determined that >40% of Sierra Negra consists of flows 1,000 years old or younger. Rowland (1996) used multiple remote sensing data sets to show that on Fernandina 134 lava flows (55% of the subaerial area) have a young appearance (low albedo, complete margins). Naumann and Geist (2000) showed that at least 30% of Cerro Azul's surface is <1,000 years old.

The two most recent Galápagos eruptions as of this writing (October 2002; Fig. 2) occurred on the SW flank of Fernandina from January to April 1995 (GVN 1995a, 1995b, 1995c, 1995d) and on the SE flank of Cerro Azul

from September to October 1998 (GVN 1998a, 1998b). Both eruptions were accompanied by minor activity in the summit calderas, but the bulk of the activity occurred on the mid to lower flanks.

Because the only permanent human habitation in the W. Galápagos is the small town of Villamil on the south coast of Isabela (Fig. 1), it is almost certain that eruptions have gone unnoticed since humans arrived in the archipelago in the mid-1500s. In fact, the earliest reported eruption is in 1813 (Simkin and Seibert 1994), almost 300 years after that first arrival. Although the human population has grown to the point that it is now unlikely that this can happen anymore, access to eruption sites is still difficult. Thus remote sensing data are a useful resource that can be added to ground-based observations, providing supplementary quantitative data and an excel-

Table 1 The 1995 Fernandina eruption

Date, time (all are 1995)	Event or observation
1/25, evening	Red light seen by tour boat and fishermen as well as geologists on Sierra Negra, who also report back lit caldera rim indicating intra-caldera activity
1/27, 09:00	Inland plume and steam plume at coast, lava entering ocean, 400-m-long new scoria cone at vent with fountains 30–50 m high, bulk effusion rate estimate $150\text{--}90\text{ m}^3\text{ s}^{-1}$
1/27, night	Large dammed-up volume of lava enters ocean and produces sudden, strong, littoral explosions
2/2	800-m-wide flow front entering ocean with 100-m-wide channel
2/4, 07:45	Steam cloud much lower, water temp. measured as high as $45\text{ }^{\circ}\text{C}$ off ocean entry
2/6, morning	Fountains restricted in extent but higher (to $\sim 150\text{ m}$)
2/11, am	Fountains still strong, distal, S part of flow is dark and moving slowly
2/13	Channels blocked, many smaller surface flows, plume extending W at 10 s/km , 1.5 km radius area of discolored water around ocean entry
2/15	Flow activity decreasing at coast, surface activity increasing inland
2/16	No flow activity at coast
2/19	No steaming at coast, fountaining diminished greatly
2/21	Two “rivers” of lava entering ocean, fountaining to 100 m
3/ 2	Lava entering ocean via tubes
3/5	Glow observed from $\sim 30\text{ km E}$
3/6, morning	Weak steam clouds along coast, water temp locally $45\text{ }^{\circ}\text{C}$ at 50 m from the shore near where lava drips into ocean, greatest flow $\sim 2\text{ km N}$ of Cabo Hammond with 2.5-m -wide channel, blue fume, hissing, and occasional spattering at vent
3/17	Three ocean-entry points with flows $0.5\text{--}1.5\text{-m}$ -wide spattering at vent to $\sim 70\text{ m}$ every few seconds, pool of lava within cone $30\text{--}40\text{ m}$ wide, flows entering upper end of tubes, no incandescence at night, but entry of lava into ocean continues (lava in tubes?)
4/8	Eruption over, total duration =73 days

lent means for monitoring eruptive activity (Harris et al. 2000). In fact, the onset of the 1998 eruption of Cerro Azul was detected in Hawai'i from GOES images $\sim 8.5\text{ h}$ before ground confirmation (Mouginis-Mark et al. 2000).

The 1995 Fernandina eruption

Fernandina began erupting during the evening of 25 January 1995. A narrative of this eruption can be pieced together from accounts and information that were at one time posted on the web site of the Charles Darwin Foundation, Global Volcanism Network (GVN) reports for January to May of 1995 (GVN 1995a, 1995b, 1995c, 1995d), and Wooster and Rothery (1997). Field observers reported glow coming from the caldera, and a new flow is visible in a SPOT scene collected 6 July 1995 (Fig. 3D). Also, early in the eruption two vents opened at elevations of $\sim 1,000$ and $\sim 750\text{ m}$ above sea level, which are at, and just below, the summit platform/outer flank boundary, respectively. These upper flank flows produced negligible volumes of lava and along with the intra-caldera lava are not part of the current study. A third vent (star, Fig. 2A) centered at $\sim 230\text{ m a.s.l.}$ produced almost all of the lava of this eruption. This vent is $\sim 4\text{ km}$ from the coastline, which the flows reached by the morning of 27 January. Channelized flows continued to enter the ocean until 8 April, the final day of the eruption. During the latter stages, parts of the channels roofed over to form tubes that delivered lava directly to the ocean. The subaerial portion of the resulting flow field is roughly triangular with the vent at the uphill apex and a width along the coast of almost 4 km (Fig. 3A). Table 1 summarizes events during the eruption.

The 1998 Cerro Azul eruption

The 1998 Cerro Azul eruption began shortly after mid-day local time on 15 September. Narratives of this eruption are given in GVN (1998a) and Mouginis-Mark et al. (2000). Preliminary maps of the 1998 caldera and flank lava flows are presented in Naumann and Geist (2000). The main flank vent became localized at $\sim 640\text{ m a.s.l.}$, $\sim 5.5\text{ km}$ from the eastern caldera rim (star, Fig. 2B). Activity continued from this vent until 21 October, generating channel-fed flows that extended about 16 km from the vent, but which did not reach the ocean. A post-eruption SPOT image (Fig. 3B) allows us to divide the flow into proximal, medial, and distal sections based on the plan-view morphology. The proximal section is broad and diffuse, measuring up to 2.5 km wide and extending 4.5 km from the vent. It is a complex of multiple, branching 'a'a flow units and numerous kīpuka, most of which are high-standing pre-existing vents. Three distinct channelized flows issued out of this diffuse proximal section, one from the center heads 4 km southeast, one from the eastern end heads $\sim 1\text{ km}$ east, and the third from the southeast part extends east (over-running the second branch) then southeast to become the main flow. It is this third branch that we have in turn subdivided into medial and distal sections. The medial section is defined by the presence of a distinct channel and totals almost 11 km in length. The flow width here varies between 300 and $1,100\text{ m}$, and the channel width between 80 and 460 m . The distal section extends only 2 km beyond the end of the distinct channel and averages $\sim 1,300\text{ m}$ in width. The most distal portion of the flow is a small branch 0.6 km long and $100\text{--}250\text{ m}$ wide. Table 2 contains a summary of events during the 1998 Cerro Azul eruption, compiled

Table 2 The 1998 Cerro Azul eruption

Date, time (all are 1998)	Event or observation
9/15, 12:29–13:04	Eight earthquakes detected
9/15, 12:58	First thermal anomaly in GOES data, eruption onset (in caldera)
9/15, 17:00	First ground reports of eruption
9/16, 04:28	Second thermal anomaly in GOES data, to the SE (on flank)
9/17, 12:30	Flank flow 8 km long, two intra-caldera flows reach edge of intra-caldera lake
9/25, 13:30	Last field confirmation of caldera activity
9/28, 18:58	Last GOES image with thermal anomaly in caldera
10/5, 12:00	Tortoises rescued from path of lava
10/11, 21:00	Last field observation of active flows
10/12, 06:28	Plume extends ~30 km from volcano
10/21, 05:28	Last saturated GOES band 2 pixel, eruption over(?) total duration =36 days

from GVN (1998a, 1998b), and Mouginis-Mark et al. (2000).

Data and methods

A 10-m spatial resolution InSAR DEM that pre-dates both the Fernandina and Cerro Azul eruptions was collected in May of 1993 by NASA's airborne TOPSAR instrument (Zebker et al. 1992; Mouginis-Mark et al. 1996; Rowland 1996). Post-eruption SAR images to which interferometric techniques can be applied were collected after both eruptions by ERS-1 and ERS-2 radars (25 m spatial resolution). The InSAR technique works only for sub-aerial surfaces. The entire 1998 Cerro Azul flow is subaerial, but an unknown amount of lava from the 1995 Fernandina eruption entered the ocean so only the subaerial flow volume can be assessed with radar data.

GOES data collected during the 1995 Fernandina eruption were not archived by NOAA, the agency that runs the satellite, and during the 1998 Cerro Azul eruption they were not archived in any form other than non-quantitative jpeg images. It is important to point out that this lack of archiving is the norm; interested users of GOES data must archive the data themselves if they intend to use them retrospectively. Unfortunately, ATSR data during the Cerro Azul eruption are too cloudy to be of use. Therefore, our only quantitative thermal data are the ATSR observations of the Fernandina eruption in 1995. Other supporting data include SPOT satellite images of both volcanoes (pre-eruption panchromatic and post-eruption color), eruption accounts published in the GVN newsletter, and discussions with colleagues who witnessed the eruptions first-hand and kindly shared their ground and airborne photos and observations.

Geophysical monitoring and measurements

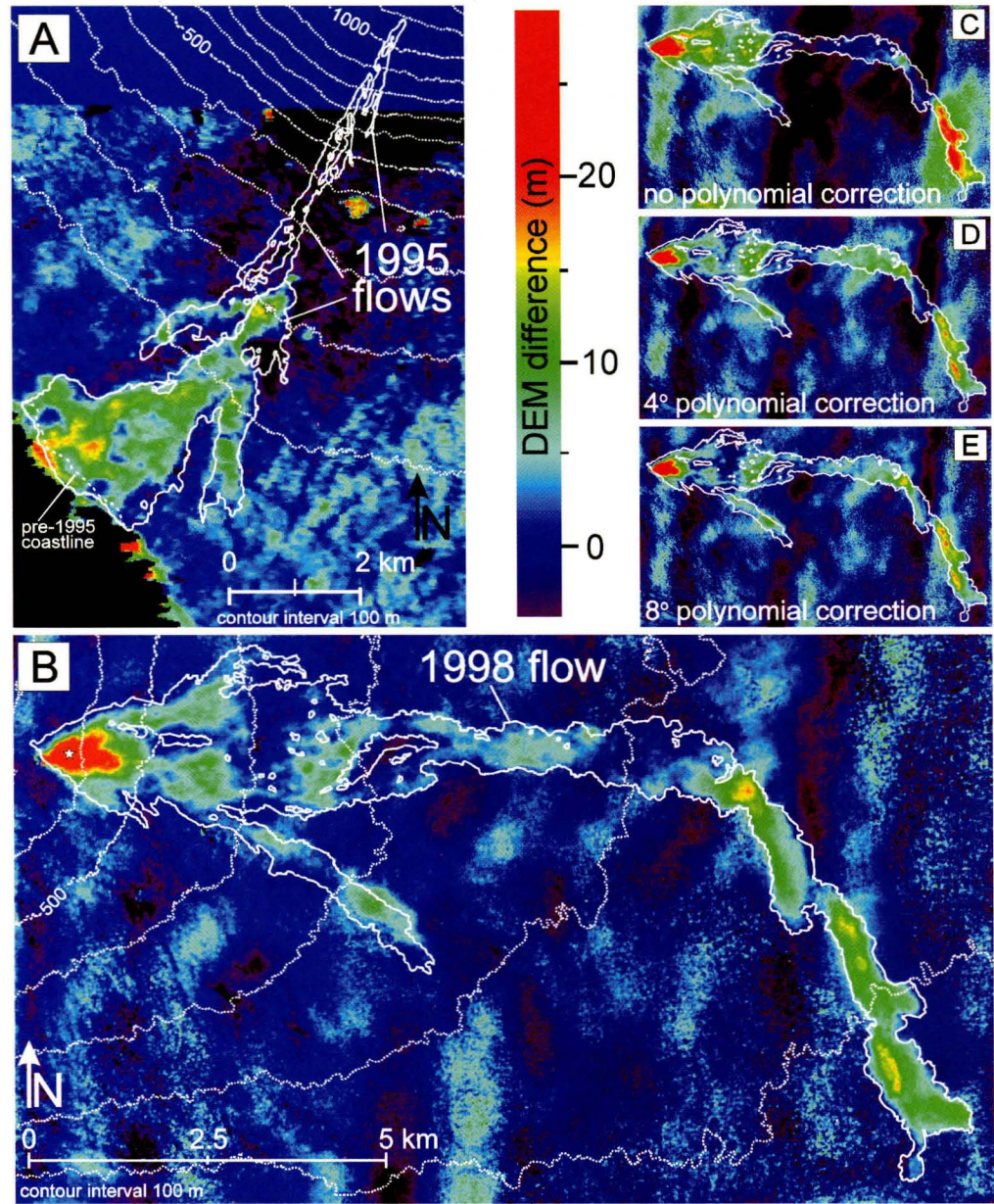
At the time of these eruptions there was essentially no geophysical monitoring of the W. Galápagos volcanoes. Prior to the Fernandina eruption, increased seismicity (including two M5 earthquakes) was reported in the vicinity of the Galápagos from December 1994 to January 1995 (GVN 1995a). None of this seismicity appears to

have been constrained sufficiently to make any connection to the Fernandina eruption. The eruption itself was monitored from the ground and offshore only intermittently (GVN 1995a, 1995b, 1995c, 1995d). Post-eruption studies include a map showing the flow location and an estimated volume (Rowland 1996), an assessment of satellite-derived active flow areas (Wooster and Rothery 1997), and studies of surface deformation produced by emplacement of the eruptive dike (Jonsson et al. 1999; Zebker et al. 2000). No continuous geophysical or geological monitoring was carried out.

The situation was improved in two ways by the time of the 1998 Cerro Azul eruption. First, the satellite-based GOES thermal anomaly monitoring system (Harris et al. 2000) was operational. Second, a seismic network had been established in the W. Galápagos about a year prior to the eruption (GVN 1997). Neither system recorded any precursory activity but both recorded the onset of the eruption (GVN 1998a; Mouginis-Mark et al. 2000). Furthermore, Cerro Azul is more accessible than Fernandina so the eruption was monitored more closely by geologists both from the ground and from the air (GVN 1998a, 1998b; Ellisor and Geist 1999). Post-eruption studies include the GOES analysis (Mouginis-Mark et al. 2000), preliminary assessment of co-eruptive deformation from interferometric radar (Amelung et al. 2000), and petrologic studies of the erupted lavas (Ellisor and Geist 1999; Teasdale 2002).

Thus, during neither of these Galápagos eruptions were systematic detailed geological or geophysical measurements collected. Additionally, other than estimates of volumetric flow rates based on channel observations (which are difficult even under the best of conditions; Pinkerton 1993), no syn-eruptive quantitative field measurements were made. Our intent here is to add retrospective quantitative volumetric and thermal data to the mostly qualitative information regarding these eruptions in order to constrain the recent eruption behavior of these volcanoes.

Fig. 4A–E Topographic change images derived by subtracting the pre-eruption TOPSAR DEM from post-eruption ERS DEMs. The data have been corrected for noise and tilts by subtracting 1° and 9° polynomial surfaces for Fernandina and Cerro Azul, respectively (see text and Fig. 7). Flow margins are based on SPOT and radar coherence data. **A** At Fernandina the greatest thickness of lava was emplaced along the coastal plain where pre-existing slopes were minimal. Some of the large thickness just offshore is due to noise in the post-eruption DEM. Roughly circular locations of large thickness outside the flow margin are obvious at elevations of roughly 200, 400, and 500 m a.s.l. Three of them correspond to pre-existing cinder cones but it is not clear why they should show such behavior in the elevation-change data. **B** In the Cerro Azul data a wave-like pattern of noise is evident, with a wavelength of approx. 1.5 km and crests and troughs running roughly north–south. Polynomial surfaces up to degree 15 were unsuccessful at removing this noise completely and it causes some of the thickness variation along the flow. **C–E** Cerro Azul thickness images showing progressive reduction of noise with increasing degree of polynomial surface used for correction



Calculating flow field area, thickness, and volume from SPOT and InSAR data

Flow field area was determined mainly with multispectral SPOT images that have a spatial resolution of 20 m (panchromatic SPOT data have 10 m spatial resolution). SPOT-1, which provided our Fernandina image, has three multispectral bands (green, red, and near-IR) whereas SPOT-4, giving our Cerro Azul image, has four (green, red, near-IR, and SWIR). For the most part these SPOT scenes (Fig. 3) allowed us to distinguish the 1995 and 1998 flows from underlying young basalts. In places, the SPOT data did not distinguish the 1995 Fernandina flow sufficiently from the pre-existing surface and other data were therefore also used to help determine the flow area (see below). Comparison with panchromatic SPOT data

collected over both volcanoes in 1988 also helped determine new flow margins.

It was difficult in places to define the boundary of the 1995 Fernandina flow because even in the multispectral SPOT image there is little spectral difference between the new flows and others nearby that are relatively recent (Fig. 3). It is also difficult to define the flow boundary using the thickness map (Fig. 4) due to noise that masks the contrast between changed and unchanged surface heights (e.g., thin flow margins are below the vertical resolution of the difference image). In some of these areas we relied on the degree of phase correlation, or coherence, between pre- and post-eruption radar images that we co-registered to the SPOT data (Fig. 5). Coherence is a measure of how similar the scattering properties of two radar image pixels are, and it depends on thermal noise,

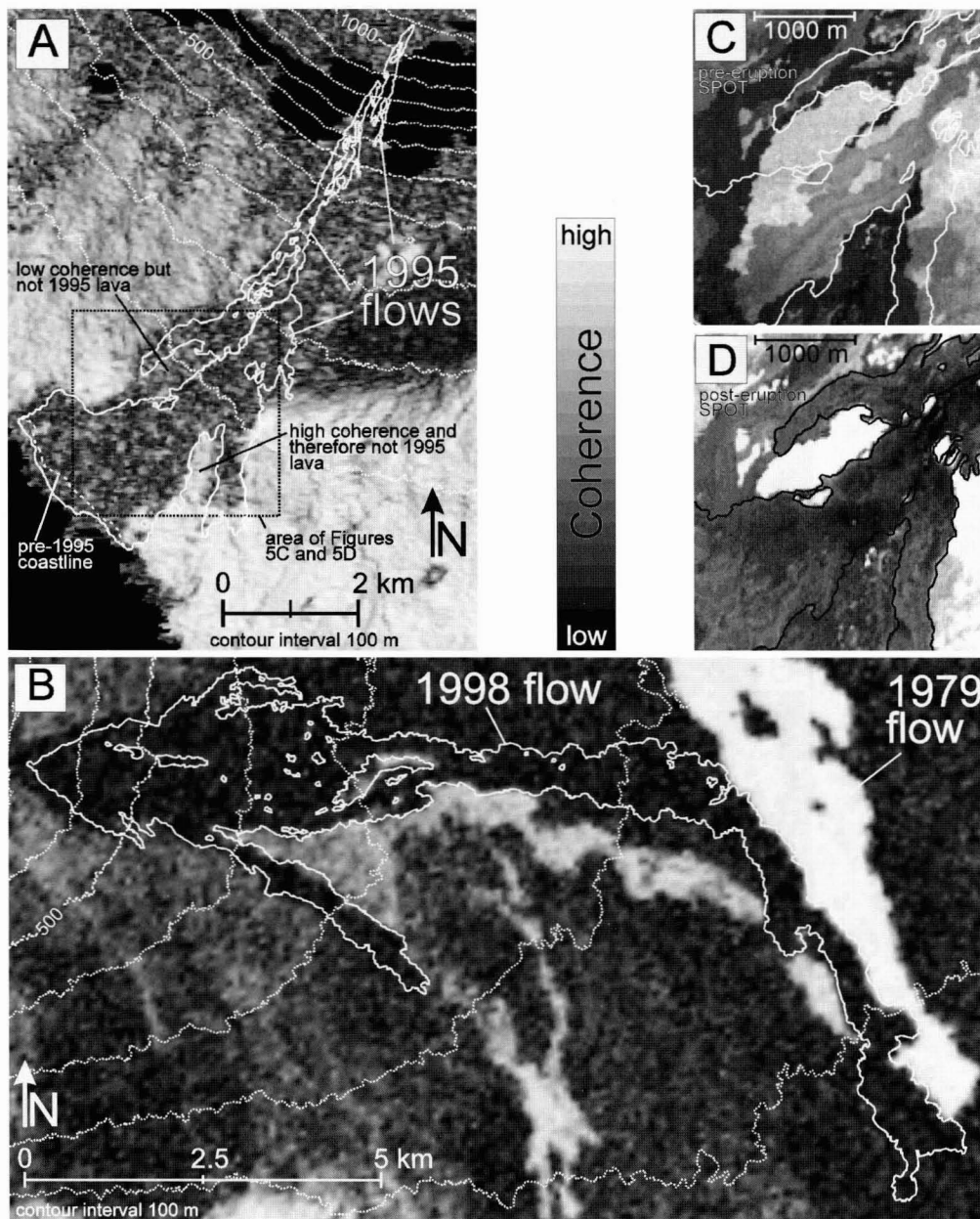


Fig. 5 Radar coherence images for both flows derived by comparing pre- and post-eruption radar images, and used to aid in determining the areas covered by new lava (flow outlines otherwise drawn mostly from SPOT data. Compare in Figs 3A and A, the region between the large flow arm near the southeastern end of the flowfield. In the SPOT data (Fig. 3A) there is little spectral contrast between the arm, the intervening ground separating the arm from the main flow, and the main flow. Indeed, Rowland (1996) mapped the intervening ground as part of the 1995 flow. In the coherence image, however (A), it is clear that this intervening ground is highly correlated; it did not change between 12 September 1992 and 30 September 1997, the dates of the ERS data used to produce this

image, and, therefore, cannot be 1995 lava. Note that, however, coherence alone cannot be used to determine the 1995 flow area. On the northwest margin is an area of low coherence between the 50 and 200 m elevations that extends up to a kilometer NW of the 1995 flow. Some of this low coherence corresponds to the distal end of the 1995 flow erupted from the 750-m vent, but much of it includes no new lava (determined by comparing the 1996 and 1988 SPOT scenes; C and D). In addition to new flows, low coherence is also associated with vegetated areas. This is illustrated in B where most of the image is vegetated. The 1998 flow cannot be discerned from the surrounding forest and the only area of high coherence corresponds to the (mostly unvegetated) 1979 flow

changes in the position of objects on the surface, and the relative orientation of the two images. Detailed discussions of radar coherence can be found in Rosen et al. (1996) and Zebker and Villasenor (1992).

InSAR-derived flow thickness and volume determination required the use of TOPSAR, ERS-1, and ERS-2 data. Two types of InSAR-based topographic change studies on active volcanoes have been undertaken recently. The first works when two radar images are

collected, one before and one after a topographic change event that consists only of vertical and/or horizontal deformation of the otherwise unchanged surface (e.g., a shallow dike or sill intrusion). In such a case, the images are well correlated, meaning that the processing software is able to recognize and then correlate pixels corresponding to the same ground locations in both images. When the two images are compared, the radar signal at each pixel, therefore, will differ only by a phase shift. This phase shift will be due to topography plus any deformation that has occurred between the time of the two image collections. A pre-existing digital elevation model (DEM) allows the topography component to be removed, allowing the deformation component to be measured at each pixel to sub-centimeter accuracy. This method was applied recently to the Galápagos by Jonsson et al. (1999) and Amelung et al. (2000). It requires pre- and post-deformation SAR images plus a pre-eruption DEM (which need not be derived from the InSAR).

Here we used a different technique because when a new lava flow is emplaced, radar pixels within the flow area obviously will not have the same surface state in pre- and post-eruption images. Instead these pixels decorrelate, meaning that they differ by more than merely being out of phase; the technique described above will not work. As shown in Fig. 5, the region of decorrelation does provide an indication of the lava flow area (see also Zebker et al. 1996). In order to determine flow volume two DEMs are required, one produced before and one produced after the eruption; topographic change (i.e., lava flow thickness) is measured by subtracting one DEM from the other. If derived from InSAR, each of these DEMs requires two radar images.

The method of producing a DEM by InSAR techniques is explained in numerous references (e.g., Zebker and Goldstein 1986; Rowland et al. 1999). We used a TOPSAR DEM that pre-dates both eruptions and post-eruption DEMs produced from ERS-1 and ERS-2 data. TOPSAR (Zebker et al. 1992) collected the pre-eruption data in May 1993. These data have a spatial resolution of 10 m and a vertical accuracy of 1–2 m; field checking over similar volcanic surfaces confirms this vertical accuracy (Rowland et al. 1999). Because TOPSAR collects the two radar signals required for interferometry simultaneously, there are no problems with temporal decorrelation in the pre-eruption DEM.

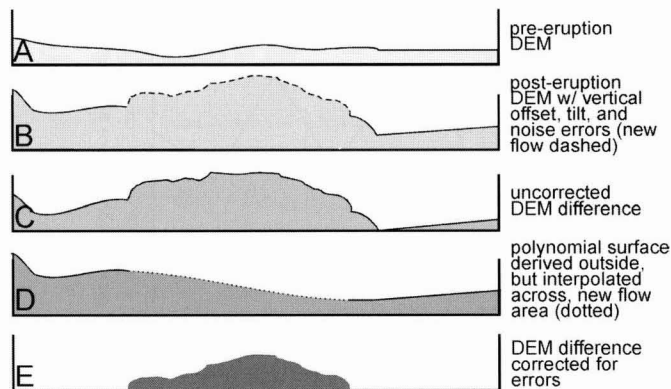


Fig. 6 Diagrams illustrating the technique of deriving a polynomial surface to correct for tilt, offset, and warp noise in DEM-difference data. Although our example shows the noise to be in the post-eruption DEM, it could be in either the pre-eruption or post-eruption DEM, or both

The ERS-1 and 2 satellites have single antennas and, therefore, can only collect a single image of a particular location per orbit. This means that the post-1995 Fernandina and post-1998 Cerro Azul DEMs each required two separate images from two different passes. By 1997, when our post-eruption InSAR data were collected (Table 3), ERS-2 was operational and flying in tandem mode with ERS-1 with a temporal separation of only hours.

The pre-eruption TOPSAR DEM was subtracted from the post-eruption ERS DEMs to give height difference images in which new lava flows show positive values (Fig. 4). Ideally, the height difference images should have values of zero everywhere except where the new flows were emplaced, but in practice there may be vertical offsets, tilts, and undulations in the DEMs (Stevens et al. 1999). This was particularly true for the post-eruption 1998 Cerro Azul case because at this time the ERS-1 satellite was reaching the end of its life and was producing noisy data (Fig. 4B). ERS-1 became completely inoperative 7 days after the 3 March 2000 image was acquired.

To obtain accurate volumes this noise must be removed. We achieved this by deriving a polynomial-defined surface (Fig. 6). This surface was generated by calculating coefficients using points in the DEM difference image in an annulus around, but not including, the new flow. This synthetic surface was next interpolated

Table 3 InSAR parameters for data used in this study

Date	Radar sensor	Track	Use
30 May 1993	TOPSAR	n.a.	Pre-eruption DEM for both Fernandina and Cerro Azul
12 September 1992	ERS-1	412	Fernandina decorrelation pair (perpendicular baseline =270 m)
30 September 1997	ERS-2	412	
30 September 1997	ERS-1	412	Post-1995 Fernandina DEM (perpendicular baseline =230)
1 October 1997	ERS-2	412	
15 June 1992	ERS-1	140	Cerro Azul decorrelation pair (perpendicular baseline =109 m)
5 November 1998	ERS-2	140	
3 March 2000	ERS-1	61	Post-1998 Cerro Azul DEM (perpendicular baseline =216 m)
4 March 2000	ERS-2	61	

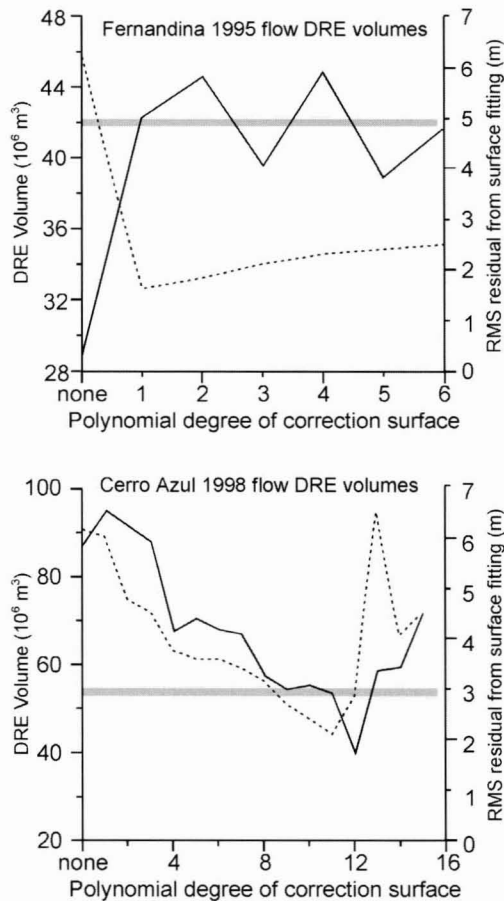


Fig. 7 Graphs of DRE flow volume (*solid line*) and RMS residual from surface fitting (*dashed line*) vs. the polynomial degree of the surface used to correct for noise in the post-eruption DEM. *Gray bars* indicate volumes reported in text. The RMS fitting residual is calculated for a ~ 30 pixel-wide annulus surrounding each flow and is the root mean square of these pixel values with respect to zero, based on the assumption that these points should have values of zero because no topographic change occurred within the annulus. **A** For Fernandina a 1° polynomial surface (a sloping plane) increases the volume from ~ 29 to $\sim 42 \times 10^6 \text{ m}^3$; increasingly complex surfaces do not produce a consistent increase or decrease in volume. The 1° surface also produces the lowest residual from surface fitting (~ 2 m). **B** For Cerro Azul, where the post-eruption DEM was much more noisy, a relatively consistent volume was not achieved until the 9th to 11th degree polynomial surfaces were applied, corresponding to a volume of $54 \times 10^6 \text{ m}^3$. These correspond to the lowest residual values from surface fitting, also ~ 2 m

across the entire image and then subtracted from the raw DEM difference image. For the Fernandina and Cerro Azul data, we produced synthetic surfaces with polynomial degrees ranging from 1 to 6 and 1 to 15, respectively. For each polynomial surface we can calculate a RMS residual value that is a measure of how well the two DEMs fit in the annulus surrounding the flow. Figure 7 compares these surface-fitting RMS values with the polynomial degree of the surface. The lowest surface-fitting residual values are around 2 m and we consider this to be the vertical uncertainty in the DEM difference data.

Integration of these adjusted thickness data within the area of the new flow produces bulk flow volumes, and these likewise are affected by the polynomial surface used to correct the DEM difference data (Fig. 7). The majority of the 1995 and 1998 flows are 'a'ā, so we used a 25% void space correction (Wolfe et al. 1987) to convert bulk volumes to dense-rock equivalent (DRE) volumes. The gray bands in Fig. 7 were chosen by eye and represent the volumes reported in Tables 4 and 5. Mean effusion rate E_{mean} , as opposed to instantaneous effusion rate (E_r ; see below), is derived by dividing DRE volume by eruption duration.

Calculating instantaneous effusion rates and flow volume from satellite-derived thermal data

As noted above, only the ATSR data (collected during the Fernandina eruption) allowed us to derive instantaneous effusion rates. Harris et al. (1997, 1998, 2000) and Wright et al. (2001) showed that the total heat loss measured from satellite data can be converted to the instantaneous effusion rate (E_r) at the time the image data were collected using

$$E_r = Q_{tot} / [\rho(Q_p \Delta T + c_L \Delta \phi)] \quad (1)$$

Q_{tot} is instantaneous heat loss from the flow (in J s^{-1} and measured from ATSR data), ρ and C_p are lava density and specific heat capacity, ΔT is eruption temperature minus solidus temperature, c_L is latent heat of crystallization, and $\Delta \phi$ is the volume percent of crystals that form while cooling through ΔT . We correct ρ and C_p to $2,600 \text{ kg m}^{-3}$ and $1,150 \text{ J kg}^{-1} \text{ K}^{-1}$, respectively, due to $20 \pm 10\%$ vesicles (after Gaonac'h et al. 1996; Herd and Pinkerton 1997), and use a value of $3.5 \times 10^5 \text{ J kg}^{-1}$ for c_L .

The changes in volume percent crystals ($\Delta \phi$), in temperature (ΔT), and in vesicularity (which has an effect on C_p) are the least constrained parameters in this treatment. Following Pieri and Baloga (1986) and Harris et al. (1997, 1998), we bracketed the ATSR-derived effusion rates and volumes by using ranges of $\Delta \phi$ (45–55%), ΔT (150–350 °C), and vesicularity (10–30%). We also define two end-member cases, a hot model and a cool model (Table 6). The hot model maximizes heat loss with high eruption, crack, crust, and base temperatures combined with a thin base. Conversely, the cool model minimizes heat loss and uses a thick base. Note that heat loss will be inversely correlated with effusion rate and, therefore, volume; if the lava is giving off more heat (the hot model), less of it is needed to produce the measured thermal response in an image pixel. Sensitivity to the range in input parameters is shown in Table 6. Increasing vesicularity by 10% causes E_r , and in turn calculated volume, to increase by 18%. Decreasing ΔT from 350 to 150 °C causes E_{peak} and calculated volume to both increase by 40%. The wide range of uncertainty results in the range of effusion rates and derived volume estimates presented below.

Table 4 Summary of eruption parameters determined for the 1995 Fernandina eruption

Parameter	Value	Method	Notes
Subaerial area	$6.5 \times 10^6 \text{ m}^2$	SPOT and SAR decorrelation	Figs. 3A, 5A
Average subaerial thickness	$8.5 \pm 2 \text{ m}$	DEM difference	Fig. 4A
Max. subaerial thickness	$\sim 25 \text{ m}$	DEM difference	Fig. 4A
Subaerial DRE volume ^a	$42 \pm 10 \times 10^6 \text{ m}^3$	DEM difference	Fig. 4A
Total DRE volume I	$27\text{--}101 \times 10^6 \text{ m}^3$	Integration under ATSR effusion rate curve	Fig. 8; Eq. 1
Mean effusion rate I	$4\text{--}16 \text{ m}^3 \text{ s}^{-1}$	Integrated ATSR volume divided by 73 days	Fig. 8; Eq. 1
Total DRE volume II	$9\text{--}23 \times 10^6 \text{ m}^3$	Sum of volumes derived from heat loss	Eq. 2
Early effusion rate	$68\text{--}90 \text{ m}^3 \text{ s}^{-1}$	Field estimate of channel dimensions	Day 2, GVN (1995a); converted here to DRE
Peak effusion rate I	$60\text{--}215 \text{ m}^3 \text{ s}^{-1}$	FLOWGO	for 7 h into eruption
Mean effusion rate II	$9\text{--}10,441 \text{ m}^3 \text{ s}^{-1}$	Dike and pressure considerations, Eq. 3	Viscosity range from 1,000–36 Pa s; Dp/dz range from 27,000 to 36,000 Pa m^{-1}

^a Uncertainty is product of flow area and residual from surface fitting (2 m) corrected to DRE

Table 5 Summary of eruption parameters determined for the 1998 Cerro Azul eruption

Parameter	Value	Method	Notes
Area	$16 \times 10^6 \text{ m}^2$	SPOT and SAR decorrelation	Figs. 3B, 5B
Average thickness	$4.5 \pm 2 \text{ m}$	DEM difference	Fig. 4B
Max. thickness	$\sim 30 \text{ m}$	DEM difference	Fig. 4B
DRE volume ^a	$54 \pm 24 \times 10^6 \text{ m}^3$	DEM difference	Fig. 4B
Mean effusion rate I	$17 \text{ m}^3 \text{ s}^{-1}$	DEM volume divided by duration	
Peak effusion rate I	$461\text{--}753 \text{ m}^3 \text{ s}^{-1}$	FLOWGO	For 7 h into eruption
Mean effusion rate II		Dike and pressure considerations, Eq. 3	Viscosity range from 1,000–36 Pa s; Dp/dz range from 27,000 to 36,000 Pa m^{-1}
1.5-m dike	$0.2\text{--}541 \text{ m}^3 \text{ s}^{-1}$		
0.65–1.07-m dike	$3\text{--}1491 \text{ m}^3 \text{ s}^{-1}$		
Mean effusion rate III	$12.8\text{--}42.6 \text{ m}^3 \text{ s}^{-1}$	Flow length relationships	Eq. 4
	$6.7 \text{ m}^3 \text{ s}^{-1}$		Eq. 5
	$47.4 \text{ m}^3 \text{ s}^{-1}$		Eq. 6

^a Uncertainty is product of flow area and residual from surface fitting (2 m) corrected to DRE

Table 6 ATSR-derived Volume, E_r , and E_{peak} parameters

Input	E_r best fit relationship	R^2	Volume from integrating best-fit curve ($\times 10^6 \text{ m}^3$)	E_r on 8 February 1995 from ATSR and Eq. (1) ($\text{m}^3 \text{ s}^{-1}$)	E_{peak} at $t=1$ min from best-fit relationship ($\text{m}^3 \text{ s}^{-1}$)
Hot model: eruption temperature (T_{erupt})=1,130 °C, crust temperature (T_c)=400 °C, hot crack temperature (T_h)=1,050 °C, flow base temperature (T_{base})=900 °C, flow base thickness (h_{base})=0.5 m					
Vesic =0.1, $\Delta T=350$	$-5.0 \ln(t)+22.1^a$	0.996	27	8.4	58.5
Vesic =0.2, $\Delta T=350$	$-6.1 \ln(t)+26.6$	0.996	33	10.2	71.0
Vesic =0.3, $\Delta T=350$	$-7.5 \ln(t)+32.9$	0.996	41	12.6	87.4
Vesic =0.1, $\Delta T=150$	$-8.4 \ln(t)+36.6$	0.996	46	14.0	97.7
Vesic =0.2, $\Delta T=150$	$-9.9 \ln(t)+43.2$	0.966	54	16.3	115.2
Vesic =0.3, $\Delta T=150$	$-11.9 \ln(t)+51.9$	0.996	65	19.9	138.4
Cool model: eruption temperature (T_{erupt})=1,100 °C, crust temperature (T_c)=75 °C, hot crack temperature (T_h)=950 °C, flow base temperature (T_{base})=580 °C, flow base thickness (h_{base})=3.0 m					
Vesic =0.1, $\Delta T=350$	$-8.1 \ln(t)+35.7$	0.996	45	13.4	94.6
Vesic =0.2, $\Delta T=350$	$-9.6 \ln(t)+42.3$	0.996	53	15.9	112.1
Vesic =0.3, $\Delta T=350$	$-11.7 \ln(t)+51.3$	0.996	64	19.4	136.4
Vesic =0.1, $\Delta T=150$	$-13.5 \ln(t)+59.3$	0.996	75	22.3	157.5
Vesic =0.2, $\Delta T=150$	$-15.6 \ln(t)+68.6$	0.996	86	25.9	182.0
Vesic =0.3, $\Delta T=150$	$-18.5 \ln(t)+81.0^a$	0.996	101	30.6	215.5

^a Plotted in Fig. 8

Vesic = vesicularity, $\Delta T = T_{erupt}$ minus solidus temperature, t = times since eruption onset in days

Net heat loss is due to the radiative and convective heat losses from the flow surface and conductive heat loss through the flow base (Oppenheimer 1991; Harris et al. 1998, 2000). These thermal calculations require knowledge of, or assumptions to be made about, the area and thermal structure of the flow surface. Wooster and Rothery (1997) assumed that each 1-km ATSR pixel is occupied by active lava (with a two component flow surface composed of crust at 75–400 °C broken by cracks at 950–1,050 °C) plus the surrounding ground at ambient temperatures. The crust and crack areas of the active lava in each pixel are then calculated from the ATSR short-wave infrared (1.6 μm) and thermal infrared (11 μm) data, respectively. Total flow volume is derived by plotting effusion rate against time and integrating over the duration of the eruption. Where necessary this plot is extrapolated to the onset of the eruption to determine E_{peak} (Table 6).

An alternative method was used by Wooster et al. (1997), based on the idea that while the flow cools from its eruption temperature (T_{erupt}) to ambient (T_{amb}), heat supplied to the surface from the interior will be balanced by heat lost by radiation, convection, and conduction. This total heat-budget method assumes that from thermal images available at both a sufficient frequency and duration during an eruption, it is possible to calculate the total radiative heat (Q_{rad}) given off by all the lava in the scene cooling from T_{erupt} to T_{amb} . Conductive (Q_{cond}) and convective (Q_{conv}) heat losses are modeled and added to Q_{rad} to give $Q_{\Delta T}$, the total heat lost from the entire flow in the image as it cools from T_{erupt} to T_{amb} . Hence we can adapt Eq. (1) so that:

$$V = Q_{\Delta T} / \{ \rho [C_p (T_{\text{erupt}} - T_{\text{amb}}) + c_L \Delta \phi] \} \quad (2)$$

We applied this technique as well, using T_{erupt} of 1,100–1,130 °C (Allan and Simkin 2000) and T_{amb} of 25 °C. The total energy budget of the flow was calculated from the ATSR data combined with the conductive and convective models, and then used in Eq. (2) to calculate V , the volume of erupted lava visible to the sensor.

Using FLOWGO to derive flow length, channel width, and instantaneous effusion rate

We used FLOWGO, a thermo-rheological model (Harris and Rowland 2001) to derive effusion rates and rheological parameters. A minimum of two inputs are required by FLOWGO: (1) the starting channel dimensions (depth and width), and (2) the ground slope over which the flow advances. Combined, these produce an at-vent effusion rate. FLOWGO then follows a lava element down-flow, calculating heat loss and flow core temperature at each 1-m increment. These quantities are in turn input into rheological calculations that determine the time required to flow the next 1-m increment, and hence a new flow velocity. Mass is conserved and channel depth held constant so this new velocity produces a new channel

width. Additionally, velocity affects flow crust characteristics, which in turn, affect heat loss amounts; these, in addition to rheological and crystal-content values, are recalculated and used to derive the next set of rheological parameters, and so on.

Thus, for given at-vent conditions FLOWGO can determine the cooling-limited channel length, plus the flow velocity and rheological and crystallinity characteristics of the lava at any point down the channel. For the two Galápagos eruptions considered here the slope profile was derived from the pre-eruption TOPSAR DEM. Similar to the method above, two end members of the FLOWGO model, termed hot and cool, utilize parameter end members that respectively maximize and minimize heat loss down flow. Included in the parameter ranges are starting eruption temperatures of 1,130 and 1,100 °C, typical of Galápagos basalts (Allan and Simkin 2000), and these are used in the hot and cold models, respectively.

For the Cerro Azul case, we determined effusion rates consistent with the observed channel length and width. We used a field-based estimate of the flow thickness (5 m, R. Ellisor, personal communication) to approximate channel depth and set the at-vent channel width equal to depth (i.e., a square cross section).

For Fernandina, however, the observable flow length ends at the coastline. Here we applied a different approach and used FLOWGO to determine an effusion rate and channel velocity consistent with the observation that lava was entering the ocean a minimum of 21 h after the eruption began (Table 1). Field observations of channel dimensions and an estimate of bulk effusion rate by J. Stimac (GVN 1995a) helped constrain the modeled effusion rate.

Mean effusion rate determined by dike dimensions, magma chamber pressure, and exponential release of accumulated strain

Mean effusion rate can also be derived from fluid dynamical considerations of the magma flowing through the feeder dike from the magma chamber to the vent. Naumann and Geist (2000) modified the Poiseuille equation for steady-state flow (mean effusion rate) of fluid between two plates once an eruptive dike has opened, to obtain

$$E_{\text{mean}} = w^3 l (dP/dz - g \rho_{\text{magma}}) / (12 \eta_{\text{magma}}) \quad (3)$$

in which dP/dz is the pressure gradient, w and l are fissure width and length, respectively, g is gravity, ρ_{magma} is magma density, and η_{magma} is magma viscosity. This equation considers only the lithostatic pressure component to magma effusion and, therefore, is applicable once elastic strain has been released. Note also that Naumann and Geist (2000) used a value of dP/dz based on the along-strike fissure length. In reality, the pressure drop occurs from the magma chamber to the surface and we

suggest that it is likely that the fissure length will underestimate this distance considerably. Therefore, we used Eq. (3) with a range of dP/dz values.

Mean effusion rate determined from flow length measurements

Effusion rate can also be derived from knowledge of lava properties, flow length, and underlying slope. Pinkerton and Wilson (1994) show that theoretically

$$L_{\text{flow}} \approx 0.242 E_{\text{mean}}^{0.64} t \alpha^{0.64} d^{-0.91} \left[(Y_s/\eta)^{1/3} \right]^{1.09} \quad (4)$$

and statistically

$$L_{\text{flow}} = 1.32 E_{\text{mean}}^{0.47} t_f^{0.71} \alpha^{0.51} d^{-0.34} \quad (5)$$

Here, L_{flow} , t , α , d , Y_s , η , and t_f are flow length, time from initiation of the flow, mean slope, mean flow thickness, lava yield strength, lava viscosity, and duration of lava supply, and $[(Y_s/\eta)^{1/3}]^{1.09}$ has a value around 0.063 and 0.136 for the distal and proximal parts of flows, respectively. Kilburn (2000) links the maximum possible flow length (L_{max}) to lava properties and E_{mean} using

$$L_{\text{max}} \approx [3 \varepsilon S / g \rho \kappa]^{1/2} E_{\text{mean}} \quad (6)$$

in which εS and κ are, respectively, energy per unit volume for the flow front to exceed its yield strength (2×10^4 Pa) and thermal diffusivity ($4.2 \times 10^{-7} \text{ m}^2 \text{ s}^{-1}$). These equations can only be applied in the Cerro Azul case because the Fernandina flow entered the ocean.

Fernandina results

Subaerial flow thickness, area, and volume

The image data (SPOT and SAR decorrelation) yield a subaerial flow field area for the 1995 Fernandina eruption of $6.5 \times 10^6 \text{ m}^2$. The average subaerial thickness is 8.5 m, and the maximum, occurring near the coast, is ~ 25 m. Integrating the difference between pre- and post-eruption InSAR DEMs produces a DRE subaerial flow volume of $42 \pm 10 \times 10^6 \text{ m}^3$. It is meaningless to produce an average effusion rate by dividing this subaerial volume by the eruption duration because of the lava that entered the ocean. Note that our measurement does not take into account the small volume of lava erupted from the higher elevation vents.

Instantaneous effusion rates and total volume determined from ATSR, FLOWGO, and field data

ATSR-derived effusion rates [Eq. (1)] range between 8 and $31 \text{ m}^3 \text{ s}^{-1}$ on day 15 of the eruption (Table 6) and decreased to $\sim 5 \text{ m}^3 \text{ s}^{-1}$ by day 73, at the reported end (Fig. 8). An exponential decline can be fit to these data

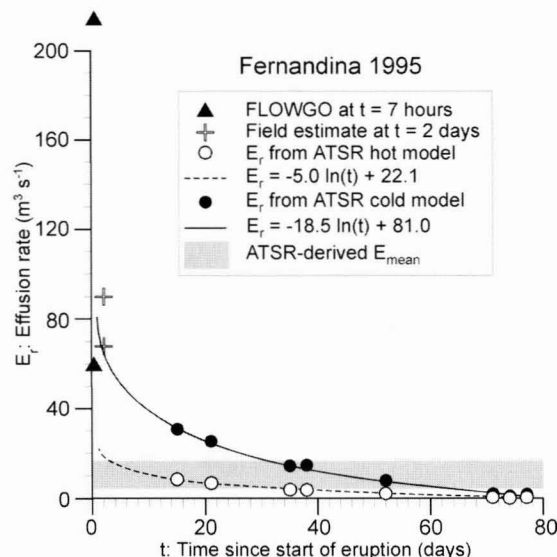


Fig. 8 Plot of effusion rates during the 1995 Fernandina eruption from ATSR, FLOWGO, and field observations. The ATSR cold (filled circles) and hot (open circles) models correspond respectively to minimum and maximum heat losses. The FLOWGO (triangles) range also corresponds to differing assumptions of heat loss (Harris and Rowland 2001). The variation in field estimates (crosses) is due to the estimated range in flow surface velocities reported in GVN (1995a)

(Table 6); however, the first 2 weeks are unconstrained and a linear effusion rate decline fits the data almost as well.

We used an effusion rate estimated in the field and FLOWGO to make up for the lack of ATSR data during the earliest stages of the eruption. J. Stimac (GVN 1995a) estimated that the channel near the vent was 10 m wide and 3 m deep and the lava surface velocity was $3\text{--}5 \text{ m s}^{-1}$, producing DRE volumetric flow rates between 68 and $90 \text{ m}^3 \text{ s}^{-1}$, if corrected for 25% vesicles (Fig. 8). These same channel dimensions can be input into FLOWGO giving peak effusion rates of $60\text{--}215 \text{ m}^3 \text{ s}^{-1}$. These values fit the exponential, but not the linear extrapolation of the ATSR-derived data (Fig. 8).

Assumption of an exponentially declining effusion rate history allows us to integrate over the eruption duration and get a total erupted volume regardless of the fact that some lava was emplaced below sea level. Integration beneath the upper (cool model) and lower (hot model) curves in Fig. 8 yields total DRE erupted volumes of 100 and $27 \times 10^6 \text{ m}^3$, respectively (Table 6). This lower ATSR total volume (the hot model) is not consistent with the $42 \times 10^6 \text{ m}^3$ subaerial volume calculated from the DEM difference, and the higher ATSR total volume indicates that as much as 58% of the lava may have been emplaced offshore. Dividing the ATSR total volume range by the 73-day eruption duration produces a mean effusion rate between 4 and $16 \text{ m}^3 \text{ s}^{-1}$.

Integrating calculated heat fluxes [Eq. (2)] over the duration of the eruption yields $Q_{\Delta T}$ of $2.8\text{--}4.4 \times 10^{16} \text{ J}$, from which Eq. (2) produces total volumes of 9–15 and

Table 7 Dependence of dike-derived E_{mean} on viscosity, fissure dimensions, and dP/dz

Viscosity (Pa s)	Dike width (m)	E_{mean} ($m^3 s^{-1}$) $dP/dz=27,000 Pa m^{-1}$	E_{mean} ($m^3 s^{-1}$) $dP/dz=31,000 Pa m^{-1}$	E_{mean} ($m^3 s^{-1}$) $dP/dz=36,000 Pa m^{-1}$
Fernandina ^a				
36 ^b	0.65–1.07	242–1,509	877–5,479	1,671–10,441
100 ^c	0.65–1.07	87–543	316–1,972	602–3,759
200 ^d	0.65–1.07	43–272	158–986	301–1,879
1000 ^e	0.65–1.07	9–54	32–197	60–376
Cerro Azul ^f				
36 ^b	0.65–1.07	7–31	58–257	121–541
100 ^c	0.65–1.07	2–11	21–93	44–195
200 ^d	0.65–1.07	1–6	10–46	22–97
1000 ^e	0.65–1.07	0.2–1	2–9	4–19
36 ^b	1.5	84	709	1491
100 ^c	1.5	30	255	537
200 ^d	1.5	15	128	268
1,000 ^e	1.5	3	26	54

^a E_{mean} range also due to fissure length (l) varying between 250 and 350 m

^b Dragoni (1993)

^c Moore (1987)

^d Naumann and Geist (2000)

^e Shaw et al. (1968)

^f Fissure length =20 m

15–23×10⁶ m³ for the hot and cold models, respectively. Q_{rad} , Q_{conv} , and Q_{cond} contribute 59–65, 23–29, and 6–18% of this total $Q_{\Delta T}$. These volumes are smaller than those derived from the other methods and this is probably because the assumption that this $Q_{\Delta T}$ is due to complete lava cooling over the time period covered by ATSR data is incorrect. That complete cooling almost certainly continued well beyond this time period is based on measurements elsewhere. For example, Wooster et al. (1997) showed that the 1991–1993 flow on Etna (which was considerably thicker than the 1995 Fernandina flow) had lost only 28% of its thermal energy by the eruption end. Incomplete cooling means that the heat measured and modeled in this technique would not in fact sum to $Q_{\Delta T}$, but some number less than $Q_{\Delta T}$, and inspection of Eq. (2) shows that this will result in a calculated volume that is too small. Additionally, because some of the heat loss occurred underwater and, thus, was not observed by the sensor, the calculated volume will be lower than that actually erupted.

Mean effusion rates calculated from dike dimensions and pressure considerations [Eq. (3)]

Field reports (Table 1) described a 400-m-long scoria cone. Allowing for deposition beyond the ends of the surface rupture we use a fissure length of 300±50 m. These are combined into Eq. (3) with a modeled dike width of 0.86±0.21 m (Jonsson et al. 1999), dP/dz values of 27,000, 31,000, and 36,000 Pa m⁻¹, magma density of 2,600 kg m⁻³, and a range of published magma viscosities. This produces E_{mean} values that range from 9 to 10,400 m³ s⁻¹ (Table 7), most of which are larger than the ATSR-derived values of 4–16 m³ s⁻¹.

Cerro Azul results

Flow area, volume, and average effusion rate

The SPOT data yield a flow length and area of ~16 km and ~16 km², respectively, and these agree with the results from SAR decorrelation (Figs. 3B and 5B). Based on the DEM difference (Fig. 4B), the average thickness is 4.5 m with the maximum of ~30 m occurring in the region of the vent. From the vent region to 10 km downflow the average thickness is 3 m whereas the last 6 km averages 8 m thick. Integrating over the DEM difference yields a DRE volume of 54±24×10⁶ m³. This is based on a 25% vesicularity correction for the entire flow, but because the thickest part (near the vent) is undoubtedly more vesicular than this, our calculated volume is a maximum. Dividing the DRE volume by the 36-day duration produces a mean effusion rate of 17 m³ s⁻¹.

Instantaneous effusion rate derived from FLOWGO

Application of the FLOWGO model gives a cooling-limited channel length of 14±2 km. This length and the modeled downflow variation in channel width are in good agreement with dimensions obtained from the SPOT image (Fig. 9A). Note that adding the ~4-km-long distal portion of the flow beyond the channel would produce a closer match to the ~16-km total flow length.

The modeled at-vent channel velocity of 24±6 m s⁻¹ gives an effusion rate early in the eruption of 460–750 m³ s⁻¹. The modeled mean velocity over the first 3 km of 11±2 m s⁻¹ is in excellent agreement with the 12 m s⁻¹ estimated in the field (Fig. 9B; R. Teasdale, personal communication). The velocity and rheological parameters determined by FLOWGO produce a Gratz number (G_z) of

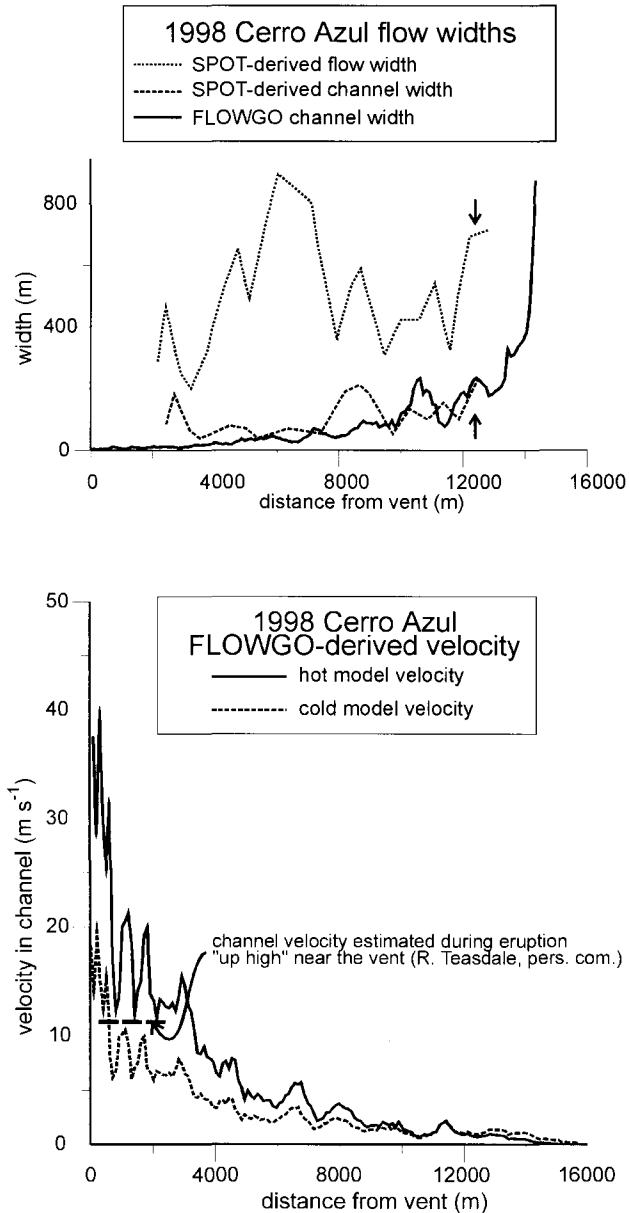


Fig. 9 **A** Comparison of Cerro Azul channel and flow widths derived from SPOT data (see Fig. 3B for measurement locations) vs. FLOWGO-derived channel widths. Note that around 12,500 m from the vent (arrows) the FLOWGO channel width increases suddenly to a value approximately equivalent to the overall flow width. It is at this point in the SPOT data that the well-defined channel no longer exists and the entire flow was moving. Essentially the flow has become the channel. **B** Flow velocities determined by FLOWGO plotted against distance from the vent. The hot and cold models in FLOWGO (Harris and Rowland 2001) maximize and minimize heat losses, respectively. The hot model, for example, requires a higher velocity (and effusion rate) in order to allow lava to flow the same distance down the channel before solidifying. Note the close agreement near the vent with a field estimate of 12 m s^{-1} .

A 233, consistent with the cooling-limited nature of the flow as $G_z < 300$ is characteristic of cooling-limited flows on Etna and Kilauea (Pinkerton and Wilson 1994).

Mean effusion rates calculated from dike dimensions and pressure considerations

Equation (3) can be used to estimate effusion rates for the Cerro Azul eruption as well. Because dike width was not measured independently as it was for the Fernandina eruption (Jonsson et al. 1999), we calculated E_{mean} using the Fernandina dike width (0.65–1.07 m) in addition to the typical dike width measured in the walls of the Cerro Azul caldera (1.5 m; Naumann and Geist 2000). Pressure gradient (dP/dz) of $36,000 \text{ Pa m}^{-1}$, fissure length (20 m), and magma density ($2,700 \text{ kg m}^{-3}$) are all from Naumann and Geist (2000), and we also include calculations for dP/dz values of $31,000$ and $27,000 \text{ Pa m}^{-1}$. As for Fernandina, the wide range of published magma viscosities produces a considerable variation in the values of E_{mean} ($< 1\text{--}1,490 \text{ m}^3 \text{ s}^{-1}$; Table 7).

B

Mean effusion rates from the 16-km flow length

Using L_{flow} and L_{max} of 16 km, t and t_f of 35.5 days, a mean slope of 3.2° obtained from the DEM, and d of 6.255 m in Eqs. (4), (5), and (6) gives E_{mean} values of 12.8–42.6, 6.7, and $47.4 \text{ m}^3 \text{ s}^{-1}$, respectively. These are in reasonable agreement with the E_{mean} of $17 \text{ m}^3 \text{ s}^{-1}$ derived by dividing the DEM-difference volume by the eruption duration.

Discussion

The eruption parameters derived from the numerous techniques above are summarized in Tables 4 and 5. Our preferred range for the subaerial volume of the 1995 Fernandina flow ($42\text{--}100 \times 10^6 \text{ m}^3$) is two to four times the $23 \times 10^6 \text{ m}^3$ average volume of all young flows erupted on the lower slope apron as determined by Rowland (1996). However, those pre-1995 flows included examples that were partially buried and in no case was the pre-eruption topography known. Rather than indicating that the 1995 flow is unusually voluminous it instead shows the importance of determining volumes by a technique that takes into account the thickness over the entire flow area rather than just the margins (e.g., Murray 1990; Stevens et al. 1999; Murray and Stevens 2000).

Data on the average areas and volumes of individual Cerro Azul flows are not available; however, comparison with Fig. 5 of Naumann and Geist (2000) indicates that the 1998 Cerro Azul flow was not unusual with respect to areal coverage.

The effusion rates we determined by the various methods vary widely (Tables 4 and 5), with E_{peak} values of 60–215 and 460–750 $\text{m}^3 \text{ s}^{-1}$ for the Fernandina and

Table 8 Mean eruption rates for selected basaltic volcanoes

Volcano (eruption year)	Mean effusion rate* ($\text{m}^3 \text{s}^{-1}$)
Fernandina (1995)	4–16
Cerro Azul (1998)	7–55
Mauna Loa (1984)	110
—(1950)	32–1044 (range for six flows)
—(1926)	100
—(1907)	47
—(1887)	212
—(1868)	95
—(1859)	208
Kīlauea (1983–1986)	20–300
—(1969)	140–400
—(1955)	28–33
—(1840)	94
Etna (2001)	16
—(1983)	6–9
—(1981)	35–55
—(1971)	13
—(1865)	8
—(1669)	92

* Most values derived by dividing total flow volume by eruption duration

Cerro Azul cases, respectively. E_{mean} ranges are 4–10,440 and 0.2–1,490 $\text{m}^3 \text{s}^{-1}$. Note, however, that some of the values of E_{mean} calculated from dike dimensions and pressure considerations [Eq. (3)], are greater than the peak effusion rates determined by a variety of other methods. Likewise they span a considerable range depending on the input viscosity and pressure gradient. We consider them to be the least useful in this regard and consider the range of E_{mean} to be 4–16 and 7–47 $\text{m}^3 \text{s}^{-1}$ for Fernandina and Cerro Azul, respectively. These are compared in Table 8 to E_{mean} values of high-fountaining-associated ‘a’ā-producing eruptions at Etna, Kīlauea and Mauna Loa. The two Galápagos eruptions have E_{mean} values similar to typical Etna values, but lower than those of typical Kīlauea and Mauna Loa eruptions.

The exponential decay in volumetric eruption rates apparent during the 1995 Fernandina eruption and inferred from our modeling of the 1998 Cerro Azul eruption is consistent with the period of waning flow defined for basaltic eruptions by Wadge (1981) and with the type I eruption rate trend defined by Harris et al. (2000). One of the values of determining peak, instantaneous, and mean effusion rates is that it allows us to use them in theoretical relationships between eruption rates and magma chamber properties. We consider two models, those of Wadge (1981) and McTigue (1987).

Following Wadge (1981), an exponential effusion rate trend can be explained by the tapping of an enclosed, pressurized system, and the decline (after an initial and short waxing phase) is due to release of elastic strain accumulated either by pressurization of the rocks surrounding the magma chamber, or by pressurization of the magma (or both). Wadge (1981) considered two end-member cases. First, that all the volume added to the magma chamber is accommodated by compression and deformation of the country rocks around and above the

magma chamber. This treatment assumed that all the surrounding rocks undergo the same amount of compression whereas it is more likely that those closest to the magma chamber will be compressed the most and those farther away compressed less. The second end-member case was that the added volume is accommodated only by compression of the magma in the chamber. This means that no surface deformation would be observed as magma is accumulated in the chamber. This is counter to observed summit deformation prior to eruptions, although Blake (1981) suggested that in some cases this assumption of constant magma chamber volume may be valid.

The treatment of McTigue (1987) can be used to develop formulae that consider accommodation of magma by both magma pressurization and deformation of the country rocks. Furthermore, it considers the decrease in country rock compression away from the magma chamber. Let a spherical magma chamber have an initial volume V_{ch} at a pressure P_{ch} . An influx of new magma with a volume dV_{extra} increases the pressure by an amount dP . The country rocks are compressed by an amount that decreases radially away from the chamber edge in such a way that an additional volume $dV_{country}$ is created where

$$dV_{country} = \frac{V_{ch}(dP)}{\mu'} \quad (7)$$

The quantity μ' is (4/3) times the rigidity modulus, μ , of the solid country rocks. The total liquid volume ($V_{ch} + dV_{extra}$) is compressed by an amount dV_{magma} where

$$dV_{magma} = (V_{ch} + dV_{extra})(dP/\beta) \quad (8)$$

and where β is the bulk modulus of the liquid magma. The extra space required to store the new magma is produced by compression of both the country rock and all the magma involved so that ($dV_{country} + dV_{magma}$) must be just equal to dV_{extra} :

$$dV_{extra} = [V_{ch}(dP)/\mu'] + [(V_{ch} + dV_{extra})(dP/\beta)] \quad (9)$$

The term involving [$dV_{extra}(dP/\beta)$] on the right-hand side can be neglected as a second-order term. The result is:

$$dV_{extra} = V_{ch}dP[(1/\mu') + (1/\beta)] \quad (10)$$

Reasonable elastic constant values are $\mu=20$ GPa, so that $\mu'=26.7$ GPa, and $\beta=10$ GPa (Fujii and Kushiro 1977). Note that the effective bulk modulus of the system, K' is equal to $[(1/\mu') + (1/\beta)]^{-1} = 7.27$ GPa.

Now let us assume that magma is erupted at the surface. Some level of excess pressure is needed to initiate the dike through which the magma passes, the amount depending on the previous history of the chamber and especially on whether any still-cooling stubs of earlier active dikes protrude from it. This threshold explains why an eruption does not start as soon as extra magma is injected into the chamber from below. If the magma chamber is located at a neutral buoyancy level, the chamber magma will be negatively buoyant in the near-surface rocks by an amount $\Delta\rho$, and an excess pressure equal to $[g h \Delta\rho]$ will be needed simply to support a static

magma column from the top of the chamber at depth h to the surface. It is only any excess pressure additional to this which is available to overcome frictional resistance to magma flow. Thus, the pressure required to feed magma to the surface, P_e , is

$$P_e = [dP - g h \Delta\rho] \quad (11)$$

Let a vertical dike feed the eruption and have horizontal length l , a horizontal width w , and a vertical height h . The flow speed of magma with viscosity η_{magma} is u where

$$u = [(P_e/h)w^2]/(12 \eta_{\text{magma}}) \quad (12)$$

so that the volume flux, $E=(u l w)$, is given by:

$$E = (P_e w^3 l)/(12 \eta_{\text{magma}} h) \quad (13)$$

What is happening here is that the excess volume dV_{extra} is being progressively erupted so that E is just maintaining a value of $[-dV_{\text{extra}}/dt]$ (the minus sign because a positive E corresponds to a decrease in dV_{extra}). Hence

$$\begin{aligned} -dV_{\text{extra}}/dt &= (P_e w^3 l)/(12 \eta_{\text{magma}} h) \\ &= ([dP - g h \Delta\rho] w^3 l)/(12 \eta_{\text{magma}} h) \end{aligned} \quad (14)$$

Now, if (and only if) $[g h \Delta\rho]$ is small enough to be neglected relative to dP , this becomes

$$\begin{aligned} -dV_{\text{extra}}/dt &= (dP w^3 l)/(12 \eta_{\text{magma}} h) \\ &= (K dV_{\text{extra}} w^3 l)/(12 \eta_{\text{magma}} h V_{\text{ch}}) \end{aligned} \quad (15)$$

which integrates to

$$V_{\text{extra}} = V_{\text{extraInitial}} \exp[-t/\tau] \quad (16)$$

$V_{\text{extraInitial}}$ is the value of dV_{extra} when the eruption starts, corresponding to an initial excess pressure dP_{Initial} , and τ is the time it takes the extra volume to decrease by e^{-1} (essentially by a third):

$$\tau = (12 \eta h V_{\text{ch}})/(K w^3 l) \quad (17)$$

To find E we differentiate Eq. (16):

$$E = [-dV_{\text{extra}}/dt] = (V_{\text{extraInitial}}/\tau) \exp[-t/\tau] \quad (18)$$

But from Eq. (16), $V_{\text{extraInitial}} \exp[-t/\tau]$ is just V_{extra} , so

$$E = (V_{\text{extra}}/\tau) \quad (19)$$

Ignoring the short-duration waxing phase of an eruption, when $t \approx 0$, E takes on its initial (and peak) value $E_{\text{Initial}}=(V_{\text{extraInitial}}/\tau)$ so we have

$$E = E_{\text{Initial}} \exp[-t/\tau] \quad (20)$$

with, using Eq. (17)

$$E_{\text{Initial}} = (V_{\text{ch}} dP_{\text{Initial}})/(K \tau) \quad (21)$$

The more general form of this in which we do not neglect the term $[g h \Delta\rho]$ follows in the same way as above, with

$$E = (V_{\text{extra}}/\tau) - [(g h \Delta\rho V_{\text{ch}})/(K \tau)] \quad (22)$$

and

$$E_{\text{Initial}} = (V_{\text{ch}}[dP_{\text{Initial}} - g h \Delta\rho])/(K \tau) \quad (23)$$

A reasonable value for $[g h \Delta\rho]$ is 4.4 MPa ($9.8 \text{ m s}^{-2} \times 1,500 \text{ m} \times 300 \text{ kg m}^{-3}$). Then if we know τ and E_{Initial} , we can rearrange Eq. (23) to solve for V_{ch} given a range of dP_{Initial} . Table 9 presents results for both the Fernandina and Cerro Azul eruptions. For Fernandina we used the effusion rate curve (Fig. 8) to derive τ and E_{Initial} (15 days and $100 \text{ m}^3 \text{ s}^{-1}$, respectively). For Cerro Azul, we used $\tau=3.6$ days based on the FLOWGO-derived E_{Initial} of

Table 9 Results of deriving magma chamber parameters from effusion rates and rate declines

dP_{Initial} (MPa)	V_{ch} (km^3)	Radius of equivalent sphere (km)	$V_{\text{erupted}}/V_{\text{chamber}}$ (%)	$V_{\text{erupted}}/V_{\text{extra}}$ (%)
Fernandina 1995				
5	1,582	7.2	0.001	3.82
10	167	3.4	0.010	18.12
15	88	2.8	0.018	22.87
20	60	2.4	0.027	25.26
25	45	2.2	0.035	26.69
30	36	2.1	0.044	27.64
35	31	1.9	0.052	28.32
40	26	1.8	0.061	28.83
45	23	1.8	0.070	29.23
Cerro Azul 1998				
5	2304	8.2	0.008	3.37
10	243	3.9	0.071	16.99
15	128	3.1	0.135	20.19
20	87	2.7	0.198	22.29
25	66	2.5	0.262	23.56
30	53	2.3	0.326	24.38
35	44	2.2	0.389	25.00
40	38	2.1	0.453	25.45
45	33	2.0	0.517	25.80

607 m³ s⁻¹ and an approximate E_{mean} of 50 m³ s⁻¹ (Table 5).

There is an inverse correlation between $dP_{Initial}$ and V_{ch} . In other words, for a given $E_{Initial}$, a low value of $dP_{Initial}$ requires a large magma chamber, whereas a high value of $dP_{Initial}$ requires only a small chamber. Note that the smaller values of $dP_{Initial}$ are probably unreasonable because they produce magma chambers with radii two to four times those of the present calderas (~3 and ~2 km for Fernandina and Cerro Azul, respectively; Munro and Rowland 1996). Second, notice that for all cases the volume of the erupted lava is less than 1% of the magma chamber volume. Finally, we can compare the volumes of the erupted lava flows to V_{extra} , the volume of magma accumulated beyond the static magma chamber volume. The two cases are similar, with 4–29% and 4–26% of V_{extra} having erupted onto the surface at Fernandina and Cerro Azul, respectively, with most of the values clustering in the 25–30% range.

At Cerro Azul, a relatively small percentage of accumulated magma erupted is consistent with the geochemical results of Teasdale (2002), who showed that it was not until late in the 1998 Cerro Azul eruption that new 1998 lava arrived at the surface. Prior to day 19 of the eruption, the composition of the lava was essentially that of the 1979 eruption and Teasdale's interpretation is that it derived from magma being flushed out of flank storage. Comparable compositional data for the Fernandina eruption are not available.

The eruptions were probably more complex than these simple exponentially declining models would suggest. Although field reports were sparse, there is some evidence that both eruptions showed effusion rate increases late in the eruptions. Teasdale (2002) noted that activity waned during the 4th week of the eruption, but then increased for another 2 weeks. It was this increase that correlated with the above-mentioned mineralogy and geochemistry changes. This may also have been the case at Fernandina, but because the eruption chronology is based on reports from three or four different observers who were each seeing the eruption for the first or second time when they made their reports, quantitative comparisons of their observations with respect to the vigor of activity are very difficult.

Conclusions

For remote, unobserved eruptions or for eruptive events for which geophysical data are sparse, we have shown how thermal infrared satellite data and numerical models can be used to obtain plausible estimates of lava flow volume and effusion rates. For the few instances where field observations can be used as ground-truth, our calculated effusion rate at Fernandina and channel velocity at Cerro Azul (Figs. 8 and 9B, respectively) compare favorably. Post-eruption optical satellite data allow derivation of flow length and width whereas InSAR data allow derivation of flow volume; all of these values

can be used as input parameters to model mean effusion rates.

Radar data in tandem with SPOT and other satellite images (e.g., ASTER, Landsat ETM+, IKONOS) can be used to obtain an accurate flow volume. In the absence of radar data, thermal data can be used to calculate flow volume, but the assumptions and uncertainties in input variables mean that the results are not well constrained. Only satellite thermal data can be used to obtain instantaneous effusion rates during an eruption and, hence, build time-averaged eruption rate curves. This points out the importance of archiving the raw radiance values derived from satellites such as GOES because it provides the highest temporal resolution of any space-based remote sensing system. These, in turn, can be used to generate insights into the plumbing system that feeds an eruptive event. The obvious best scenario is to have both radar and thermal data sets.

The present-day (October 2002) situation is already better than it was during the two Galápagos eruptions considered here because GOES data are now routinely archived and because other sensors such as MODIS are collecting high temporal-resolution thermal data. The InSAR-derived volume situation will improve as soon as the global DEM derived by the Shuttle Radar Topography Mission is available, although the 30- or 90-m spatial resolution of these data will lead to less precise volume calculations. Additionally, new radar satellites such as ENVISAT will improve our ability to produce post-eruption DEMs.

Acknowledgements This manuscript benefited greatly from very useful reviews by Geoff Wadge and an anonymous person. The work presented here was supported by NASA Grant no. NAG5-9038 from the Shuttle Radar Topography Mission (S.K.R., H.G., and P.J.M.-M.), the Leverhulme Fdn. (A.J.L.H.), NASA Grant no. NAG5-9413 (A.J.L.H.), NSF Grant no. EAR-0003542 (F.A. and S.K.R.), and the NERC Earth Observation Science Initiative (M.J.W.). ATSR data are courtesy of RAL/NERC/BNSC/ESA. This is SOEST Publication no. 6079 and HIGP Contribution no. 1255.

References

- Allan JF, Simkin T (2000) Fernandina Volcano's evolved, well-mixed basalts: mineralogical and petrological constraints on the nature of the Galápagos plume. *J Geophys Res* 105:6017–6041
- Amelung F, Jonsson S, Zebker H, Segall P (2000) Widespread uplift and "trapdoor" faulting on Galápagos volcanoes observed with radar interferometry. *Nature* 407:993–996
- Barberi F, Carapezza ML, Valenza M, Villari L (1993) The control of lava flow during the 1991–1992 eruption of Mt. Etna. *J Volcanol Geotherm Res* 56:1–34
- Blake S (1981) Volcanism and the dynamics of open magma chambers. *Nature* 289:783–785
- Chadwick WW, De Roy T, Carrasco A (1991) The September 1988 intracaldera avalanche and eruption at Fernandina volcano, Galapagos Islands. *Bull Volcanol* 53:276–286
- Crisp JA (1984) Rates of magma emplacement and volcanic output. *J Volcanol Geotherm Res* 20:177–201
- Dragonì M (1993) Modeling the rheology and cooling of lava flows, ch 9. In: Kilburn CRJ, Luongo G (eds) *Active lava flows*. University College Press, London

- Dvorak JJ, Dzurisin D (1993) Variations in magma supply rate at Kilauea Volcano, Hawaii. *J Geophys Res* 98(B12):22255–22268
- Ellisor R, Geist D (1999) 1998 Eruption at Cerro Azul, Galapagos Islands. *EOS* 80(46 Suppl):F1088
- Fujii T, Kushihiro I (1977) Density, viscosity and compressibility of basaltic liquid at high pressures. In: Annual report of the director 1976–1977. Geophysics Laboratory, Carnegie Institute of Washington, DC, pp 419–424
- Gaonac'h H, Stix J, Lovejoy S (1996) Scaling effects on vesicle shape, size and heterogeneity of lavas from Mount Etna. *J Volcanol Geotherm Res* 74:131–153
- GVN (1995a) Global Volcanism Network monthly bulletin for January 1995. *GVN* 20 no 1:2–3
- GVN (1995b) Global Volcanism Network monthly bulletin for February 1995. *GVN* 20 no 2:11–14
- GVN (1995c) Global Volcanism Network monthly bulletin for March 1995. *GVN* 20 no 3:13–14
- GVN (1995d) Global Volcanism Network monthly bulletin for May 1995. *GVN* 20 no 5:4
- GVN (1997) Global Volcanism Network monthly bulletin for August 1997. *GVN* 22 no 8:10
- GVN (1998a) Global Volcanism Network monthly bulletin for August 1998. *GVN* 23 no 8:2
- GVN (1998b) Global Volcanism Network monthly bulletin for September 1998. *GVN* 23 no 9:4–5.
- Harris AJL, Rowland SK (2001) FLOWGO: a kinematic thermo-rheological model for lava flowing in a channel. *Bull Volcanol* 63:20–44
- Harris AJL, Blake S, Rothery DA, Stevens NF (1997) A chronology of the 1991 to 1993 Etna eruption using AVHRR data: implications for real time thermal volcano monitoring. *J Geophys Res* 102:7985–8003
- Harris AJL, Flynn LP, Keszthelyi L, Mouginiis-Mark PJ, Rowland SK, Resing JA (1998) Calculation of lava effusion rates from Landsat TM data. *Bull Volcanol* 60:52–71
- Harris AJL, Flynn LP, Dean K, Pilger E, Wooster M, Okubo C, Mouginiis-Mark P, Garbeil H, Thornber C, De la Cruz-Renya S, Rothery D, Wright R (2000) Real-time satellite monitoring of volcanic hot spots. In: Mouginiis-Mark P, Crisp J, Fink J (eds) Remote sensing of active volcanism. *Geophys Monogr Ser* 116:139–159
- Harris AJL, Pilger E, Flynn LP, Garbeil H, Mouginiis-Mark PJ, Kauahikaua J, Thornber C (2001) Automated, high temporal resolution, thermal analysis of Kilauea volcano, Hawaii, using GOES-9 satellite data. *Int J Remote Sensing* 22(6):945–967
- Harris AJL, Pilger E, Flynn LP (2002a) Web-based hot spot monitoring using GOES: what it is and how it works. *Advances in environmental monitoring and modeling* (<http://www.kcl.ac.uk/kis/schools/hums/geog/advemmm/vol1no3.html>)
- Harris AJL, Pilger E, Flynn LP, Rowland SK (2002b) Real-time hot spot monitoring using GOES: case studies from 1997–2000. *Advances in environmental monitoring and modeling* (<http://www.kcl.ac.uk/kis/schools/hums/geog/advemmm/vol1no3.html>)
- Herd RA, Pinkerton H (1997) Bubble coalescence in basaltic lava: its impact on the evolution of bubble populations. *J Volcanol Geotherm Res* 75:137–157
- Holcomb RT (1987) Eruptive history and long-term behavior of Kilauea Volcano. *USGS Prof Pap* 1350:261–350
- Jonsson S, Zebker H, Cervelli P, Segall P, Garbeil H, Mouginiis-Mark P, Rowland S (1999) A shallow-dipping dike fed the 1995 flank eruption at Fernandina volcano, Galapagos, observed by satellite radar interferometry. *Geophys Res Lett* 26:1077–1080
- Kauahikaua J, Margriter S, Lockwood J, Trusdell F (1995) Applications of GIS to the estimation of lava flow hazards on Mauna Loa Volcano, Hawai'i. In: Rhodes JM, Lockwood JP (eds) Mauna Loa revealed. *Geophys Monogr* 92:315–325
- Kilburn CRJ (2000) Lava flows and flow fields. In: Sigurdsson H, Houghton B, McNutt SR, Rymer H, Stix J (eds) *Encyclopedia of volcanoes*. Academic Press, San Diego, pp 291–305
- Lipman PW (1995) Declining growth of Mauna Loa during the last 100,000 years: rates of lava accumulation vs. gravitational subsidence. In: Rhodes JM, Lockwood JP (eds) *Mauna Loa revealed*. *Geophys Monogr* 92:45–80
- McBirney AR, Williams H (1969) Geology and petrology of the Galapagos Islands. *Mem Geol Soc Am* vol 118
- McTigue DF (1987) Elastic stress and deformation near a finite spherical magma body: resolution of the point source paradox. *J Geophys Res* 92(B12):12931–12940
- Moore HJ (1987) Preliminary estimates of the rheological properties of 1984 Mauna Loa lava. *US Geol Surv Prof Pap* 1350:1569–1588
- Moore JG, Mark RK (1992) Morphology of the island of Hawaii. *GSA Today* 2:257–262
- Mouginiis-Mark PJ, Rowland SK, Garbeil H (1996) Slopes of western Galapagos volcanoes from airborne interferometric radar. *Geophys Res Lett* 23:3767–3770
- Mouginiis-Mark PJ, Snell H, Ellisor R (2000) GOES satellite and field observations of the 1998 eruption of Volcan Cerro Azul, Galapagos Islands. *Bull Volcanol* 62:188–198
- Munro DC, Rowland SK (1996) Caldera morphology in the western Galapagos volcanoes and implications for volcano eruptive behavior and mechanisms of caldera formation. *J Volcanol Geotherm Res* 72:85–100
- Murray JB (1990) High-level magma transport at Mount Etna volcano, as deduced from ground deformation measurements. In: Ryan MP (ed) *Magma transport and storage*. Wiley, London, pp 357–383
- Murray JB, Stevens NF (2000) New formulae for estimating lava flow volumes at Mt. Etna Volcano Sicily. *Bull Volcanol* 61:515–526
- Mutlow CT, Murray MJ, Smith DL, Watts PD, North P (1999) New data sets for climate change and land use studies are on track. *EOS Trans Am Geophys Union* 80(49):589–595
- Naumann T, Geist D (2000) Physical volcanology and structural development of Cerro Azul Volcano, Isabela Island, Galapagos: implications for the development of Galapagos-type shield volcanoes. *Bull Volcanol* 61:497–514
- Oppenheimer C (1991) Lava flow cooling estimated from Landsat Thematic Mapper infrared data: the Lonquimay eruption (Chile, 1989). *J Geophys Res* 96:21865–21878
- Pieri DC, Baloga S (1986) Eruption rate, area, and length relationships for some Hawaiian lava flows. *J Volcanol Geotherm Res* 30:29–45
- Pinkerton H (1993) Measuring the properties of flowing lavas, ch 6. In: Kilburn CRJ, Luongo G (eds) *Active lava flows*. University College Press, London
- Pinkerton H, Wilson L (1994) Factors controlling the lengths of channel-fed flows. *Bull Volcanol* 56:108–120
- Reynolds RW, Geist D, Kurz MD (1995) Physical volcanology and structural development of Sierra Negra volcano, Isabela Island, Galapagos Archipelago. *GSA Bull* 107:1398–1410
- Rosen PA, Hensley S, Zebker HA, Webb FH, Fielding EJ (1996) Surface deformation and coherence measurements of Kilauea Volcano, Hawaii, from SIR-C radar interferometry. *J Geophys Res* 101(E10):23109–23125
- Rowland SK (1996) Slopes, lava flow volumes, and vent distributions on Volcán Fernandina, Galapagos Islands. *J Geophys Res* 101(B12):27657–27672
- Rowland SK, Garbeil H (2000) Slopes of oceanic volcanoes. In: Mouginiis-Mark P, Crisp J, Fink J (eds) *Remote sensing of active volcanism*. *Geophys Monogr* 116:223–247
- Rowland SK, Munro DC (1992). The caldera of Volcan Fernandina: a remote sensing study of its structure and recent activity. *Bull Volcanol* 55:97–109
- Rowland SK, Walker GPL (1990) Pahoehoe and aa in Hawaii: volumetric flow rate controls the lava structure. *Bull Volcanol* 52:615–628
- Rowland SK, MacKay ME, Garbeil H, Mouginiis-Mark PJ (1999) Topographic analyses of Kilauea Volcano, Hawai'i, from interferometric airborne radar. *Bull Volcanol* 61:1–14
- Shaw HR, Wright TL, Peck DL, Okamura R (1968) The viscosity of basaltic magma: an analysis of field measurements in Makaopuhi lava lake, Hawaii. *Am J Sci* 266:225–264

- Simkin T (1972) Origin of some flat-topped volcanoes and guyots. *Mem Geol Soc Am* 132:183–193
- Simkin T, Seibert L (1994) *Volcanoes of the world*, 2nd edn. Geoscience, Tucson
- Stevens NF, Wadge G, Murray JB (1999) Lava flow volume and morphology from digitised contour maps: a case study at Mount Etna, Sicily. *Geomorphology* 28:251–261
- Teasdale R (2002) Lavas of the 1998 eruption at Volcán Cerro Azul, Galápagos: flow emplacement and magma petrogenesis. PhD Thesis, University of Idaho
- Trusdell FA (1995) Lava flow hazards and risk assessment on Mauna Loa Volcano, Hawaii. In: Rhodes JM, Lockwood JP (eds) *Mauna Loa revealed*. *Geophys Monogr* 92:327–336
- Wadge G (1977) The storage and release of magma on Mount Etna. *J Volcanol Geotherm Res* 2:361–384
- Wadge G (1981) The variation of magma discharge during basaltic eruptions. *J Volcanol Geotherm Res* 11:139–168
- Wolfe EW, Garcia MO, Jackson DB, Koyanagi RY, Neal CA, Okamura AT (1987) The Puu Oo eruption of Kilauea Volcano, episodes 1–20, January 3, 1983, to June 8, 1984. *US Geol Surv Prof Pap* 1350:471–508
- Wooster MJ, Rothery DA (1997) Time-series analysis of effusive volcanic activity using the ERS Along Track Scanning Radiometer: The 1995 eruption of Fernandina Volcano, Galápagos Islands. *Remote Sensing Environ* 62:109–117
- Wooster MJ, Wright R, Blake S, Rothery DA (1997) Cooling mechanisms and an approximate thermal budget for the 1991–1993 Mount Etna lava. *Geophys Res Lett* 24:277–3280
- Wright R, Blake S, Harris AIL, Rothery DA (2001) A simple explanation for the space-based calculation of eruption rates. *Earth Planet Sci Lett* 192:223–233
- Zebker HA, Goldstein R (1986) Topographic mapping from interferometric SAR observations. *J Geophys Res* 91(B5): 4993–4999
- Zebker HA, Villasenor J (1992) Decorrelation in interferometric radar echoes. *IEEE Trans Geosci Remote Sensing* 30:950–959
- Zebker HA, Madsen SN, Martin J, Wheeler KB, Miller T, Lou Y, Alberti G, Vetrella S, Cucci A (1992) The TOPSAR interferometric radar topographic mapping instrument. *IEEE Trans Geosci Remote Sensing* 30:933–940
- Zebker HA, Rosen P, Hensley S, Mouginiis-Mark PJ (1996) Analysis of active lava flows on Kilauea Volcano, Hawaii, using SIR-C radar correlation measurements. *Geology* 24:495–498
- Zebker HA, Amelung F, Jonsson S (2000) Remote sensing of volcano surface and internal processes using radar interferometry. In: Mouginiis-Mark P, Crisp J, Fink J (eds) *Remote sensing of active volcanism*. *Geophys Monogr Ser* 116:179–205